ETH
Eidgenössische Technische Hochschule Zürich
Swiss Federal Institute of Technology Zurich

Optimisation of a Quantitative Wide-Field-of-View Phase-Contrast Computed-Tomography Setup

Master Thesis

Simon Spindler

September 14, 2020

Advisors: Prof. Dr. M. Stampanoni, Dr. M. Rawlik , Dr. Z. Wang
Department of Physics, ETH Zürich

Abstract

Breast cancer is the most common cancer for women. To improve the reliability of early stage diagnostics differential phase contrast computed-tomography imaging is pursued at PSI where a prototype imaging grating-interferometry-breast-computed-tomography (GI-BCT) system is operated. The prototype was optimised in the areas of the acquisition protocol and the flat-field correction as well as a dedicated comprehensive simulation framework was set up. The improvements reduced the acquisition time from 11 to 9 minutes and have lead to a significant reduction in imaging artefacts. These developments bring the prototype closer to an eventual clinical application.

Acknowledgement

First, I wish to thank Professor Marco Stampanoni for giving me the opportunity to pursue a master thesis within his group.

I want to thank my supervisors Dr. Zhentian Wang and Dr. Michał Rawlik for their support throughout the thesis. Even though the year 2020 had many obstacles for all of us they always had time to teach and guide me. Especially Michał who introduced me to the system and guaranteed I could continue with the thesis even through the lock-down.

To the GI-BCT team as well as the whole group I want to thank for the interesting discussions during my stay.

Finally, to my family and girlfriend I want to express my gratitude for their patience with me and their support through all this time.

Contents

Chapter 1

Introduction

Thanks to scientific development and increasing medical knowledge over the last millennia the life expectancy in human society has been climbing well over 80 years for some countries [1]. With increasing age of the population, diseases become more prominent as well. Cancer is nowadays after cardiovascular diseases the second largest cause of death worldwide [2]. It was estimated that in 2017 around 9.5 million people died of cancer [2]. To put that in perspective, of the around 65'000 people who died in Switzerland in 2016 over 17'000 deaths were caused by cancer [3]. For women, breast cancer is the most often diagnosed type of cancer overall [4]. Because of increased awareness and prevention campaigns, breast imaging tools like mammography, computer tomography, magnetic resonance imaging (MRI) and ultrasound imaging are today important tools to diagnose breast cancer at an early stage. For this reason and improvements in cancer treatment, the five-year survival rate increased over the last years up to 90% in the U. S. [5]. In Germany, as in many level-4-income countries [6], every woman between 50 and 69 will receive an invite every two years for a mammography to diagnose and treat cancer as early as possible [7]. It is estimated that the yearly revenue of such diagnostic systems will surpass 2.5 billion dollar by 2024 [8, 9] due to breast cancer becoming a more acknowledged problem globally.

1.1 Diagnosis

The survival rate of cancer in general is often coupled to the stage it is detected at. For breast cancer it is therefore advised to undergo a regular check-up for women over 45 [10]. These check-ups include palpation, mammography and as a follow-up magnetic resonance imaging (MRI) or breast computed tomography (BCT). Mammography is one of the most often used diagnostic tools to detect breast cancer [11] as it is quick and relatively cheap,

especially compared to MRI. A mammography is the procedure to take an x-ray projection image of the breast. On this image medical doctors are able to see possibly malicious tissue which has to be examined further in case of a finding (through biopsy, etc.). The examination can be painful as the breast needs to be squeezed thin (see section 1.2.1) which causes some women to shy away from this examination method. An additional issue is the fact that a projection is often not very representative of how structures look like in 3D. This tissue overlap can cause false positive results and therefore stress and costs for patients due to further examinations. BCT is also a transmission based x-ray imaging method. This technique creates a 3D reconstruction of the breast and can therefore give a more exact view of structures in the breast compared to single projections where the 3D structures may not be obvious. The disadvantage of this method is that it is not as optimized to find so called micro calcifications [12] (which may be an early sign for cancer) as the mammography. This will be discussed in section 1.2. Another method to BCT is MRI. It has the big advantage of not using ionizing radiation as the source of information but magnetic fields. The disadvantage is its high cost and it takes significantly longer to do a measurement with an MRI system (order of tens of minutes) to around 12 seconds for a BCT (plus positioning resulting in a few minutes for the whole procedure).

1.2 Beer Lambert Law

The Beer Lambert law describes how much a photon flux decreases per length. This is the basis for absorption-based imaging. By equating the change of the number of photons dN to the number of photons in a depth dx in a material one gets:

$$dN = -\mu N dx, \tag{1.1}$$

where μ is the linear attenuation coefficient (LAC). The solution to this equation is the Beer Lambert law:

$$N = N_0 e^{-\mu x}. \tag{1.2}$$

The physical dimension of the exponent has to vanish and therefore the μ has the dimension one over meter. This LAC is material- and energy-dependent. It defines how much of the radiation gets absorbed per distance travelled through the material.
In x-ray imaging the detector measures the photon flux. When combining this flux together with a reference measurement of the full flux without a sample in the beam, the exponential term can be calculated. This exponential factor is composed out of the thickness of the material the photon flux

travelled through as well as the attenuation coefficients of all tissues crossed. The more photons the objects absorbs, the darker the region on the detector (or the brighter in the typical negative images seen in hospitals). This works well for materials with ”large” LAC differences like bone and muscle but not for the breast screening where the different types of soft tissue have a very similar LAC.

1.2.1 Attenuation Coefficients

Absorption-based x-ray imaging of the breast and especially mammographs operate at low photon energies where the difference in LAC is much larger than for high energies. Therefore the difference in absorption between the different tissues is better visible. Another advantage of low energies is that micro calcifications [12], which can be a sign of cancer, are well visible at these energies. An often used quantity is the mass attenuation coefficient (MAC) which is the LAC divided by the density of a material. For calcium the MAC is in the order of 0.9 $\frac{cm^2}{g}$ at 40 keV to 7 $\frac{cm^2}{g}$ at 20 keV while for breast tissue this value ranges from 0.25 $\frac{cm^2}{g}$ at 40 keV to 0.69 $\frac{cm^2}{g}$ at 20 keV [13] which are typical energy ranges to perform screenings [14]. This demonstrates that the lower the energy, the better the contrast.

The drawback from that technical necessity of using low energetic x-rays is that the breast needs to be squeezed thin enough such that photons are still able to reach the detector. The requirement to deposit a major fraction of the ionizing radiation in the tissue limits at the same time the amount of contrast reachable. The high absorption rate requirement does not mean that a mammography is more damaging to the tissue than higher energy x-ray images as the dose is adjusted accordingly. This only implies that the amount of signal is physically limited by the amount of radiation used and imposes a limit to absorption based imaging with ionizing radiation.

1.3 Differential Phase Contrast

Another mechanism of obtaining images through exposure to X-rays is using refraction rather than attenuation, called X-ray differential phase contrast (DPC) imaging.

The DPC is an optical effect with photons in the keV regime. The DPC image is a representation of the local deflection of the x-ray light by the sample. The refraction laws well-known in the optical regime apply also to x-rays, albeit the deflection angles are typically much smaller and refraction coefficients negative for most materials. The idea of optics also carries over that the photons deliver the information only through refraction instead of absorption, allowing this technique to not have a dose requirement at all

(although there will always remain some) compared to absorption based imaging.

1.3.1 Refraction

The most important law of refraction optics is the Snell's law. Since photons always take the fastest path between two points, in one single medium this path will be a straight line through both points. If both points now lie in different media, the path length now has to be minimized taking the speed of light in different media, expressed by the refracion index, into account. This gives the law of Snell:

$$n_1 \sin \varphi_1 = n_2 \sin \varphi_2. \tag{1.3}$$

Taking a closer look at the refractive index we can extend our definition of the refractive index to a complex refractive index:

$$n = 1 - \delta + \imath\beta \quad , \tag{1.4}$$

where δ models phase shifts and β attenuation. Plugging this into a complex wave function yields separate terms for the phase shift and attenuation:

$$\psi(x) = \psi_0 e^{\imath(1-\delta)kx} e^{-\beta kx} \quad , \tag{1.5}$$

which shows the interpretation of δ to be the phase shift and β the attenuation (same idea as explained in section 1.2) clear and makes the effects directly comparable. Looking at a transition from vacuum to water, at 20 keV $\beta \sim 4 \cdot 10^{-10}$ while $\delta \sim 5.8 \cdot 10^{-7}$ which shows that the refraction effect should be around 1000 times stronger than the absorption [15]. With higher energies this difference will further increase in favour of the phase.

The refractive indices of materials are quite different for visible light compared to x-rays. They tend to go to one for all materials, the higher the photon energy as the factors β and δ get smaller and smaller (β has discontinuities in its spectrum as the photons will start to ionize new atomic shells resulting in a sudden sharp increase of the parameter). Depending on β and δ, the refractive index for x-rays can even be slightly lower than one. This can be used for total reflection to bundle light and causes convex shapes to focus light and concave to disperse it, the opposite to the visible spectrum. The values of β and δ can be close together, through propagation in space even small differences become measurable.
This is an enormous advantage over absorption-based imaging as the image quality can be improved by solely optimising the geometry of the setup.

The physical limitation of refraction is the wavelength used as we need a wavelength smaller than the examined structure to resolve it.

Although the refraction values outperform the attenuation approach, it does not yet provide the full picture. Absorption-based imaging is compared to DPC imaging a rather simple approach which solely needs a x-ray tube and a detector to work. We do not need any optics as the photons go straight through the sample and have to be counted afterwards. Then, the attenuation can be calculated. To obtain the information of the phase either a coherent source or grating interferometry needs to be utilized. Grating interferometry solution is using optical interferometry which is phase-sensitive. The limitation of the DPC imaging method is the necessity to use interferometry to gain access to the phase information and hence to have coherence. Since there is no x-ray laser that could be reasonably used as a medical source to cover the female risk population, one such solution is grating interferometry. Gratings for x-rays are difficult to produce. In order to achieve high sensitivity to small refraction angles the high energetic x-rays need small grating pitches and in addition a deep grating structure to interact sufficiently. These challenges increase in difficulty the higher the photon energy. Even though the phase should yield a much larger signal for x-rays, engineering problems arise which are hard to solve. In contrast to absorption based imaging this is not a physical limit and allows for a development beyond the ability of absorption based imaging.

1.3.2 Talbot Lau Interferometer

As it will be shown in chapter 2.1 the gantry used for this thesis is based on the principle of a Talbot Lau interferometer. It allows to measure the DPC without a coherent source. A Talbot Lau interferometer uses three gratings to gain access to the phase information. Two gratings are absorption gratings and one is a phase grating. As it can be seen on figure 1.1 the first grating, called g0, is an absorption grating, which creates a partially spatial coherence. The phase grating g1 will produce a Talbot carpet and the absorption grating g2 is used as the analyser of the Talbot carpet.

The Talbot pattern is a periodic pattern of lines. The pattern has the same origin as the double slit pattern on a screen but instead of two slits a whole grid is used. This can be achieved with absorption gratings or diffraction gratings. Absorption gratings are made out of absorbing material such that photons can only pass through the slits and after Huygens principle, if the slit has the same dimension as the wavelength of the photon, a circular wave will exit the slit. For two slits a interference pattern with one intensity maximum in the middle will occur. For a full grating as mentioned above a Talbot carpet will occur. Absorption gratings absorb a large fraction of the incident photon field where a grating minimises these losses. A phase grat-

ing on the other hand is a diffraction grating where the photon flux is not reduced much. The diffraction pattern is created by shifting the phase of the photons relative to each other by a factor of π and causes an interference pattern through phase shift instead of absorption.

With the same method as for the double slit the maxima and minima for the Talbot pattern can be calculated. If Δ represents the path difference between two slits in the grating, we get (for a far away screen, e. g. θ small)

$$\Delta = d \cdot \sin\theta = \begin{cases} n \cdot \lambda & \text{for maxima} \\ (n + \frac{1}{2}) \cdot \lambda & \text{for minima} \end{cases} \tag{1.6}$$

with $n \in \mathbb{Z}$. The pattern repeats at the Talbot length $L_{Talbot} = \frac{2 \cdot d^2}{\lambda}$ for $\lambda \ll d$ [16].

As the information of the Talbot pattern is not directly measurable for x-rays, the analyser grating g2 is used to probe the interference pattern at the detector. The information can then be assessed by moving g0 or g2 and measuring the periodic intensity curve.
By the superposition of two periodic patterns (Talbot carpet and g2) the Moiré effect can help resolve the signal. The Moiré effect occurs when two periodic patterns are superposed resulting in measurable intensity shifts often much larger than any of the two periodicities. This magnifying effect allows to measure shifts smaller than the analyser grating pitch or even detector pixel size [17]. Making use of the Moiré effect is not a necessity. If the detector pixel would be small enough or the analyser grating had the same periodicity as the Talbot pattern, there would not be a Moiré pattern and the detector could still measure the intensity shift.

Figure 1.1 explains how it is possible to measure interference effects with a incoherent source and how to detect it. The goal of imaging is to measure as many photons as possible to reduce imaging time and get enough statistics on the measured intensity curve which will be described in section 1.3.3. Since g0 needs to block light to be able to create spatially coherent sources, the grating has to be an absorption grating. However, g1 is illuminated by many single coherent sources and therefore only has to create diffraction which can also be done with a phase grating instead, where the phase of the photons gets shifted instead of absorbed. This reduces absorption further and allows for more statistics. G2 on the other hand has to be an absorption grating to probe the Talbot carpet.

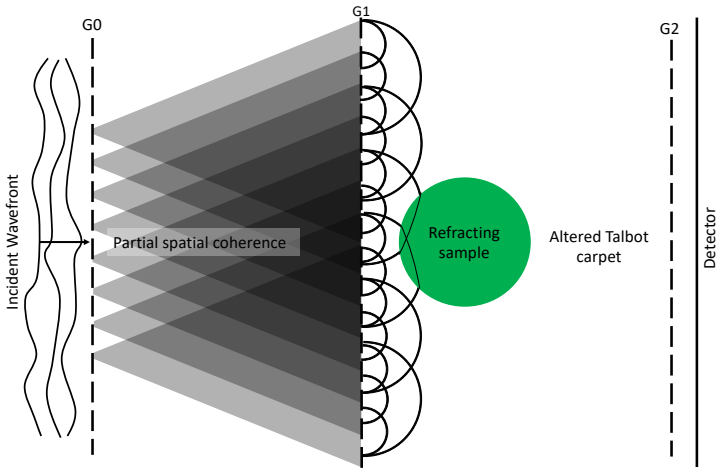

Figure 1.1: The schematic shows the effect of the different gratings on the photon field. The first grating g0 produces for each slit a for itself spatially coherent source which can produce an interference pattern after the second g1. The resulting pattern of a single slit is a Talbot carpet and by choosing the right g0 and g1 pitches, the Talbot patterns of the single slits overlay constructively without the necessity to interfere with each other. The pattern can then be probed by a third grating at a Talbot distance by moving the first or third grating. If a sample is placed before or behind the second grating, the Talbot pattern at the third grating and therefore the signal at the detector will change.

1.3.3 Differential Phase Contrast Parameters

The information from the Moiré pattern can then be transformed to attenuation, phase and dark field signal. To do so the measured intensity curve of each pixel has to be fit to a cosine as it is visualised in fig. 1.2.

The mathematical model is then:

$$I(x) = I_0(\mu)(0.5 \cdot visibility \cdot \cos(x + phase) + 0.5). \tag{1.7}$$

In this equation x represents the analyser grating position in terms of the Moiré pattern, $I_0(\mu)$ is the amplitude (times two) or absorption, visibility is the signal strength of the Moiré pattern and the phase represents the refraction induced by a sample (Note: as discussed later these values have to be corrected with the flat-field to obtain the measurements).

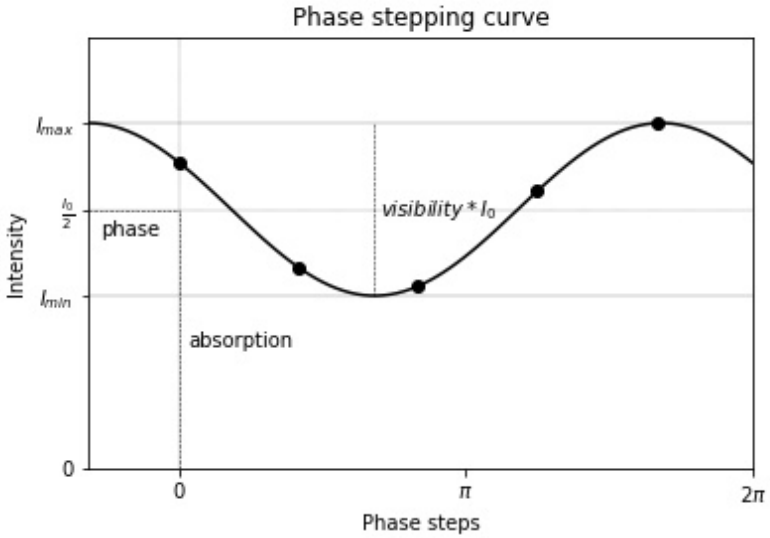

Figure 1.2: The parameters absorption, phase and visibility are shown schematically. The absorption represents the mean photon count over various phase steps by the analysing grating. The phase represents the phase offset to zero and the visibility is the difference between the highest and lowest point of the curve or strength of the DPC signal.

1.4 Computed Tomography

The goal of measuring projections at many angles is to reconstruct a 3D image out of all the projections. The underlying mathematical principle was found by Radon [18]. The principles described in the next two subsections loosely follow the introduction of the book "Medical Imaging Systems" [15].

1.4.1 Radon Transform

Radon realised that for every two dimensional shape or function, there exists a unique representation that can be obtained by straight line integrals. To ensure uniqueness of all line integrals polar coordinates can be used:

$$p(\theta, s) = \int \int_{-\infty}^{\infty} f(x,y)\delta(x\cos\theta + y\sin(\theta) - s)dxdy \quad , \tag{1.8}$$

where $f(x,y)$ is the function of the object, θ is the angle to the x-axis of the perpendicular direction to the line integral and s defines the distance of the straight line integral to a parallel line through the origin. A sketch of this equation can be seen in figure 1.3.

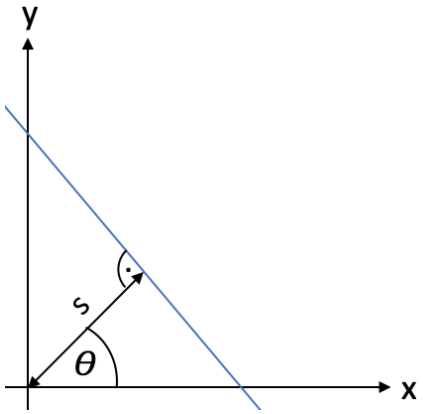

Figure 1.3: Sketch of the Radon transform. With the chosen parameters θ and $s = x\cos(\theta) + y\sin(\theta)$ all the possible lines in the 2D space are uniquely defined with the value range of $\theta \in [0,\pi]$ and $s \in [-\infty, +\infty]$.

For a fixed θ, $p_\theta(s)$ represents the projection of the object function $f(x,y)$. If all the projections at all angles are taken, the resulting plot is a sinogram as it can be seen in figure 1.4.

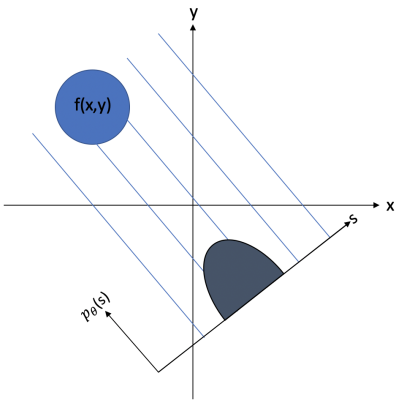

(a) A sketch of how the parameters of figure1.3 define a projection.

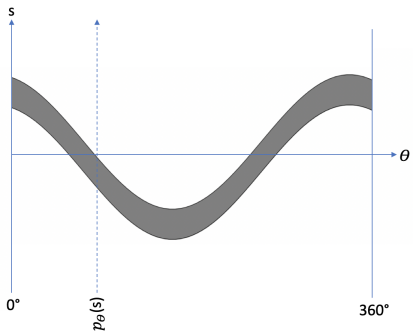

(b) If $p_\theta(s)$ is plotted over θ the resulting plot will be a so called sinogram.

Figure 1.4: If the projection $p_\theta(s)$ in the right image is taken for all angles the resulting sinogram includes all information of the Radon transform and therefore the object function $f(x,y)$. On the right image the sinogram is plotted over the full period. For this instance of a homogeneously linear projection, the full Radon transform is already given by $\theta \in [0,\pi]$. The transform can be adjusted to not be homogeneous but conical where the sinogram periodicity is then in general 2π instead of π.

The Radon transformation will therefore turn each line integral into a single value for each s and θ and changes the object function to a sinogram. The objective of computer tomography is to apply the inverse Radon transformation and recover the object function by measuring the integral lines for all s and θ which means for absorption-based x-ray imaging measuring the attenuation. The principle also works for phase contrast. The refractive index of the object will change the photon phase along the propagation direction and thus also represents a line integral of the refractive index along the path (instead of attenuation).

1.4.2 Fourier Slice Theorem

Going from the projection back to the object function or vice versa is the principle of the Fourier slice theorem. It states that a projection of a two dimensional function is the equivalent as doing a Fourier transform and slicing it through the origin (for the Radon transform at the angle θ).

With

$$\begin{aligned} F(u,v) &= \hat{f}(x,y) \\ P(\xi,\theta) &= \hat{p_\theta}(s) \end{aligned} \tag{1.9}$$

where $\hat{}$ denotes the Fourier transform of a function the equality can be recovered through:

$$\begin{aligned} P(\xi,\theta) &= \textstyle\int_{-\infty}^{+\infty} p_\theta(s) e^{-2\pi i \xi s} ds \\ &\overset{\text{eq. 1.8}}{=} \textstyle\int_{-\infty}^{+\infty} \int \int_{-\infty}^{+\infty} f(x,y)\delta(x\cos\theta + y\sin\theta - s)dxdy\ e^{-2\pi i\xi s} ds \\ &= \textstyle\int \int_{-\infty}^{+\infty} f(x,y) e^{-2\pi i(x\cos\theta + y sin\theta)\xi} dxdy \end{aligned}$$

and with variable substitution $u = \xi\cos\theta$ and $v = \xi\sin\theta$

$$P(\xi,\theta) = \textstyle\int \int_{-\infty}^{+\infty} f(x,y) e^{-2\pi i(xu+yv)} dxdy$$

it follows

$$P(\xi,\theta) = F(\xi\cos\theta, \xi\sin\theta) = F_{polar}(\xi,\theta). \tag{1.10}$$

1.4.3 Cone-Beam Geometry

The Radon transform can also be utilized when the chosen geometry does not consist of straight parallel lines but a conical line arrangement. To simplify the transformation the conical center can be fixed on the line through the origin. Therefore the line shape will be mirrored on this axis. The geometrical configuration is shown in figure 1.5.

For imaging only the space which fully includes the object function $f(x, y)$ is important and the geometry can be reduced to only the conical region of interest. Therefore, if a cone-beam x-ray tube is used instead of a photon field with a singular wave vector, the computed tomography is still possible, but the phase-space of θ now has a periodicity of 2π instead of π. If the imaging is done in 2D (e. g. with a 2D projection image instead of a 1D line) the stacking of the vertical axis needs to be done at the height where all data is available, which is not necessarily the same as the pixel height of the detector.

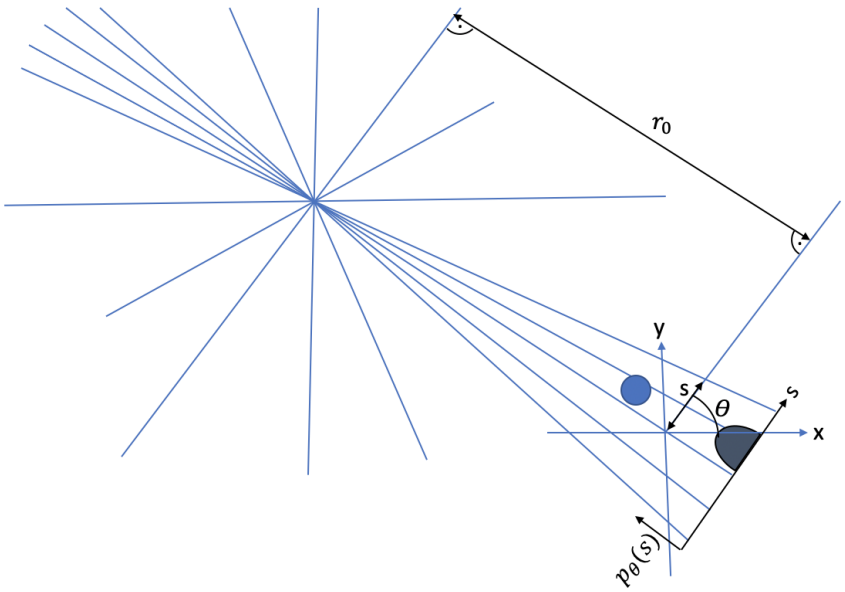

Figure 1.5: Sketch of the Radon transform in a conical configuration. Each point in space is still uniquely defined by line integrals except for the point where all lines meet.

1.5 Aim of Thesis

The experiments and data analysis contained in this thesis were performed with the aim to optimise the data quality and acquisition time. Starting point was a pre-existing wide-field-of-view grating interferometry setup with tomography protocols. In these data, artefacts were known to be present and needed to be removed. To improve the understanding of the system a data analysis was performed and simulation was used to reproduce existing features in the data. These insights were the starting point to optimise the data quality by improvement of the data acquisition script. To improve the acquisition script further the option of performing measurements while moving a grating has been examined.

Chapter 2

Materials and Methods

This chapter will introduce the hardware aspect of imaging, the data acquisition script, the flat-field correction and some tomography results from the start of the thesis.

2.1 Gantry

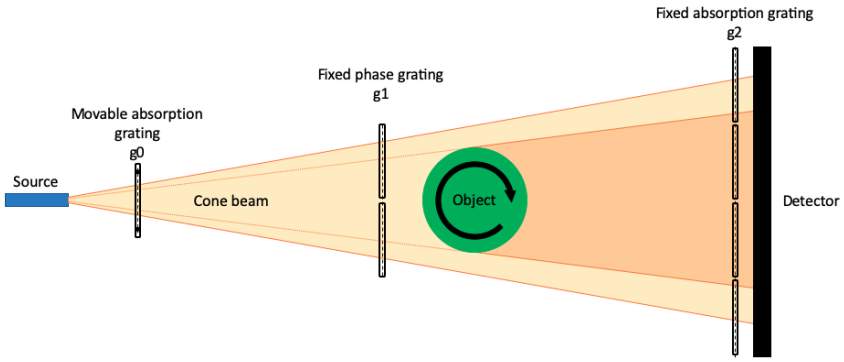

Figure 2.1: A schematic image of the gantry system used for this thesis. It consists of a source with a cone beam, three gratings g0, g1 and g2, where g0 is moved to obtain the phase information, an object holder which can rotate and move up and down to perform tomographies, as well as a detector. In the actual system the gratings and the detector are curved in the horizontal plane to be perpendicular to the cone beam.

A gantry is defined as a supportive metal frame that can hold equipment. In medical imaging devices it is referred to the part that holds the radiation source and detector with the imaging area in between.

As figure 2.1 illustrates, the system is a wide field of view cone beam grating interferometer where the whole sample cross section is scanned at once (to avoid inconsistencies and difficult image analysis). The x-ray source used throughout the thesis is a Comet MXR-225HP/11 x-ray tube. It has a focal spot size of 1 or 0.4 mm^2 and its conical photon field fully covering the sensitive area of the detector.

The grating periods, thickness and dimensions are listed in table 2.1.

gratings	absoption type I (g0)	phase (g1)	absorption type II (g2)
period [μm]	4.8	6.47	9.92
gold heigth [μm]	150	9.2	150
duty cycle	0.5	0.5	0.5
dimensions (L x W) [mm x mm]	45 x 10	80 x 17	80 x 40

Table 2.1: Parameters of the different grating types used for the gantry system.

The gratings were manufactured by the company *micro works* with the LIGA process. The absorption gratings g0 and g2 are made of gold on a graphite substrate and the phase grating g1 is gold on a silicon substrate. The gratings were bent along the vertical axis after fabrication to allow the conically emitted photons to hit the gratings as perpendicular as possible. G0 is a single grating piece of the type I absorption grating. The full phase grating g1 consists of two phase gratings which meet in the middle of the field of view. For the grating g2, 4 of the type II absorption gratings were used, where the panel two and three meet again in the middle of the field of view. The geometrical layout of the grating plates is also sketched in figure 2.1. Since moving g2 would be challenging to do accurately for such a large and heavy grating with its frame, the smallest and single panel grating g0 is moved instead to get access to the phase information as it is noted in figure 2.1. G0 is moved by a N-472 piezoelectric-motor of the company "Physik Instrumente" with a accuracy in the order of 50 nanometres (which is far below the step sizes used for g0, which are in the order of 0.8 μm). The sample holder is positioned behind g1 as sketched in figure 2.1 and consists of a container contraption for the sample, a motor to rotate the sample and a vertical motor to move the sample with the container in and out of the photon beam. Behind g2 is the photon counting detector XC-Thor by

the company "XCounter". The detector is a direct-conversion single photon-counting device with Cadmium Telluride as the active medium. This allows to keep the dose distribution to patients as low as possible. The detector has 256 x 3072 pixels with 100 μm side length and its wide field of view allows measurements of whole sample slices at once. It can take images with low frame rates and go up to several hundred Hertz. The detector is a dual energy photon counter and by changing the energy threshold of the detector the energy range of the counted photons can be adjusted. With this feature absorption edges can be measured.

Compared to absorption based tomography systems, differential phase contrast imaging requires gratings which are difficult to produce and directly limit the quality of the image. Since x-ray optics need to be able to interact with the photons to influence them, the gratings need to be thick enough to do so, while the pitch also needs to be small enough to diffract them. This combination makes the gratings difficult to produce. A lot of work is done in the field of grating fabrication [19] and with improved gratings the DPC systems will improve in data quality while absorption based imaging stagnates in development due to the underlying physical process used.

2.2 Measurements

As described in section 2.1 the systems parameter space which can be controlled for image acquisition consists of the source, the g0 positioning, the sample holder motors and the detector variables.

For the measurements the source is operated with a focal spot size of 0.4 mm^2 to maximise the spatial coherence behind g0. The spot size influences the photon statistics by limiting the current in the filament of the x-ray tube. To reach high enough photon counts the tube is operated with 70 kVp at 10 mA which was not changed throughout the thesis.

The g0 grating is controlled by a piezo motor and has a precision in the order of fifty nanometres. It can be moved at any point during a measurement. For all the tomographies contained in this thesis, the g0 was not moving while measuring. The impact of moving the piezo during image acquisition was then explored in section 7. For the phase step measurements there were usually 5 equidistant positions of g0 used in one phase period.

The sample holder position defines the magnification factor as well as the rotation center. The sample holder is composed of a vertical motor and one for rotation. The total volume that can be imaged is $(\pi \times (radius of container)^2 \times 23cm^3)$. For tomographies the acquisition procedure is to measure the volume in vertical, overlapping vertical positions and obtain all relevant phase information for all angles (mostly 600 to 1000 equidistant angles). This is accomplished by rotating the sample continuously at a speed synchronised

with the detector frame rate to obtain all angles (for most measurements the sample was rotated at one rotation per minute). These slices were then stitched together in data analysis to obtain the full volume.

The variables controlled by the acquisition script are the piezo position at all times, the rotation speed and height of the sample holder as well as the frame rate and energy threshold for the detector. In addition the tube acceleration voltage can be changed manually. The detector is able to have frame rates up to multiple hundreds of Hz. Lower frame rates need to be realized by summing over images as the counting variable limit of a pixel is limited. Due to the direct detection it is possible to use dynamic energy ranges controlled by software and is therefore also able to detect absorption edges of elements. The energy threshold for all measurements mentioned in this thesis was set to be all photons at 25 keV.

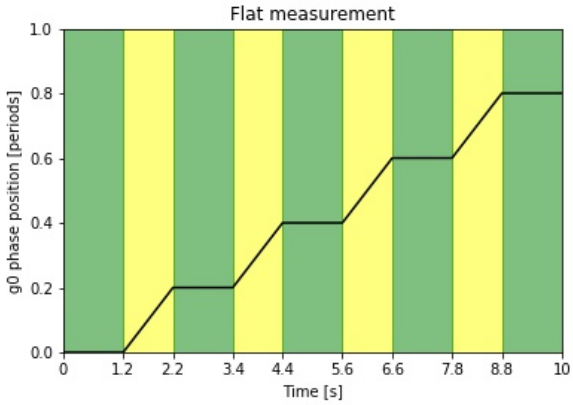

Figure 2.2: The image shows the parameter values over time to acquire a flat-field measurement. The total exposure time of the flat-field measurement is 10 seconds. The colors on the image refer to the detector and the x-ray source is always turned on. The green color means that the detector is taking images. Yellow refers to the detector not taking images. Therefore from the colors it is directly visible that the flat measurement utilizes only 6 of the 10 seconds of the exposure. The four seconds where no images are taken come from the phase steps. To ensure that g0 has reached its destination, for each phase step a waiting time of one second was implemented.

Tomographies were performed by measuring the volume in vertical segments and for each segment all angular data was acquired with all phase information directly (no helical scan). The frame rate for the measurement was 10 Hz without frame summing at a rotation speed of one revolution per minute (RPM). This results in images at 600 different angles. The sam-

ple was rotated continuously and the g0 grating was only moved while no images were taken. The phase information was gathered by measuring the sample at five equidistant phase locations of one period of g0 resulting in a total exposure of five minutes per measured slice as sketched in figure 2.3.

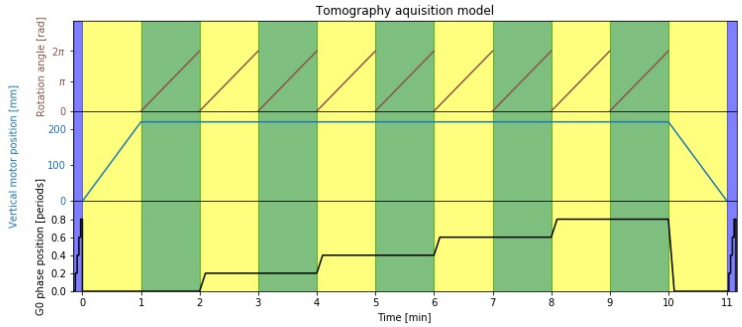

Figure 2.3: The image shows the parameter utilization to acquire all necessary information to reconstruct the tomography of a single vertical segment. The image has three rows for each motor used in the tomography. On the top row the rotation motor movement is shown, in the middle row the vertical motor and on the bottom the piezo movement. The x-ray source is always turned on. The color blue refers to a flat measurement introduced in figure 2.2, green refers, as for the flat acquisition, to the detector taking images while yellow refers to times at which the detector is not taking images. Therefore at first of the tomography segment a flat is taken, then the sample is moved into position and the sample starts while the x-ray source is turned on and the detector starts taking images at a frame rate of 10 Hz. This results in 600 projections over the angle of 2π. Then a phase step is performed while the sample keeps turning. At the same time the x-ray source is disarmed and the the detector stops taking images. This is due to the waiting time for the piezo, the script rotates the sample back to the first angle and continues the measurement there. This continues for all five phase steps. Afterwards, the sample is moved out of the field of view and another flat is measured. This script can be stacked to obtain 3D volumes larger than the detector height.

In between each segment usually two reference images (which are called flat-field images from now on) were taken before and after the measurement of the sample with a exposure of 10 seconds as sketched in figure 2.2.

The acquisition protocol for tomographies shown from here on will follow the described pattern described in figure 2.3 if not explicitly stated otherwise.

2.3 Flat-Field Correction

To obtain the signal induced by the sample, the measurements need to be compared to measurements without a sample in the beam. This is called the flat-field correction. By doing so the intrinsic imperfections of the system by the source field, the gratings and the detector can be extracted from the data at the same time. A flat is in the context of this thesis defined as the image parameters of intensity, phase and visibility obtained by analysing the data obtained from a phase stepping measurement without a sample in the beam path. Each data channel can then be corrected separately. As discussed in section 1.3.2 the absorption is the attenuation similar to classical X-ray imaging. As the attenuation is an exponential process, the correct for the flat-field the correct absorption Λ is obtained by

$$\mu = -\log\left(\frac{\Lambda_{Flat}}{\Lambda_{Data}}\right). \tag{2.1}$$

The phase φ:

$$\varphi = \varphi_{Data} - \varphi_{Flat}. \tag{2.2}$$

When cyclic values are added or subtracted to and from each other this can lead to wrapping around the 0-2π range. Therefore the phase needs to be corrected for shifts outside of [0,2π).

The visibility χ can be used to obtain the dark field Δ channel by the same formula as for the attenuation:

$$\Delta = -\log\left(\frac{\chi_{Flat}}{\chi_{Data}}\right). \tag{2.3}$$

With these three equations each pixel of the image can then be corrected for the flat-field. Each projection now shows the sample in the different channels. To go from the single projections to the 3D volume a reconstruction has to be performed. The principle of this process was introduced in section 1.4. The ASTRA package [20, 21] was used for reconstruction. the correct geometrical parameters (cone-beam, distance source-rotation centre, distance rotation centre-detector, angles and detector pixel geometry) where a Hilbert filter [22] was applied to the phase channel before reconstruction.

2.4 Initial Situation

In this section measurement results of the system will be introduced as they were at the beginning of the thesis. They serve as a reference to the results

of the thesis. In order to do so the reconstructed absorption and phase images of three different samples are shown for comparison. These samples consisted of a pig neck, a goat sausage and a human breast which was preserved. These samples are shown in figures 2.4, 2.5 and 2.6.

The phase images of the samples had a Hilbert filter applied to them before reconstruction. The Hilbert filter has a integrating nature and is an all-pass filter which means noise at all frequency are visible in the reconstruction. Absorption on the other hand has mostly high frequency noise. By rescaling images to smaller sizes, this serves as a low-pass filter which improves perceived the image quality. However, it is important to note that these absorption images are qualitatively worse than images from systems designed to do absorption imaging only as there are no gratings in between the source and detector to decrease the statistics.

These images were taken as described in section 2.2 and flat-field corrected according to section 2.3.

2.5 Outlook

The pig neck and breast images have a strong feature at the rotation axis. For absorption, this feature is contained only to the close region of the rotation center. The absorption images also show ring-like artefacts in the case that the sample extends through the rotation centre. For the phase images the artefact is centred at the rotation centre but also extends quite far into the image for some regions. For some slices the artefact gets stronger from top to the bottom resulting in almost triangular shapes which are particularly well visible in the side view of the pig neck and the human breast sample. The sausage images do not feature strong artefacts as the other two samples do but is also does not extend through the rotation centre.
These artefacts are very dominant in the central region of the image and the cause of it will be investigated in the following chapters by data analysis and simulation.

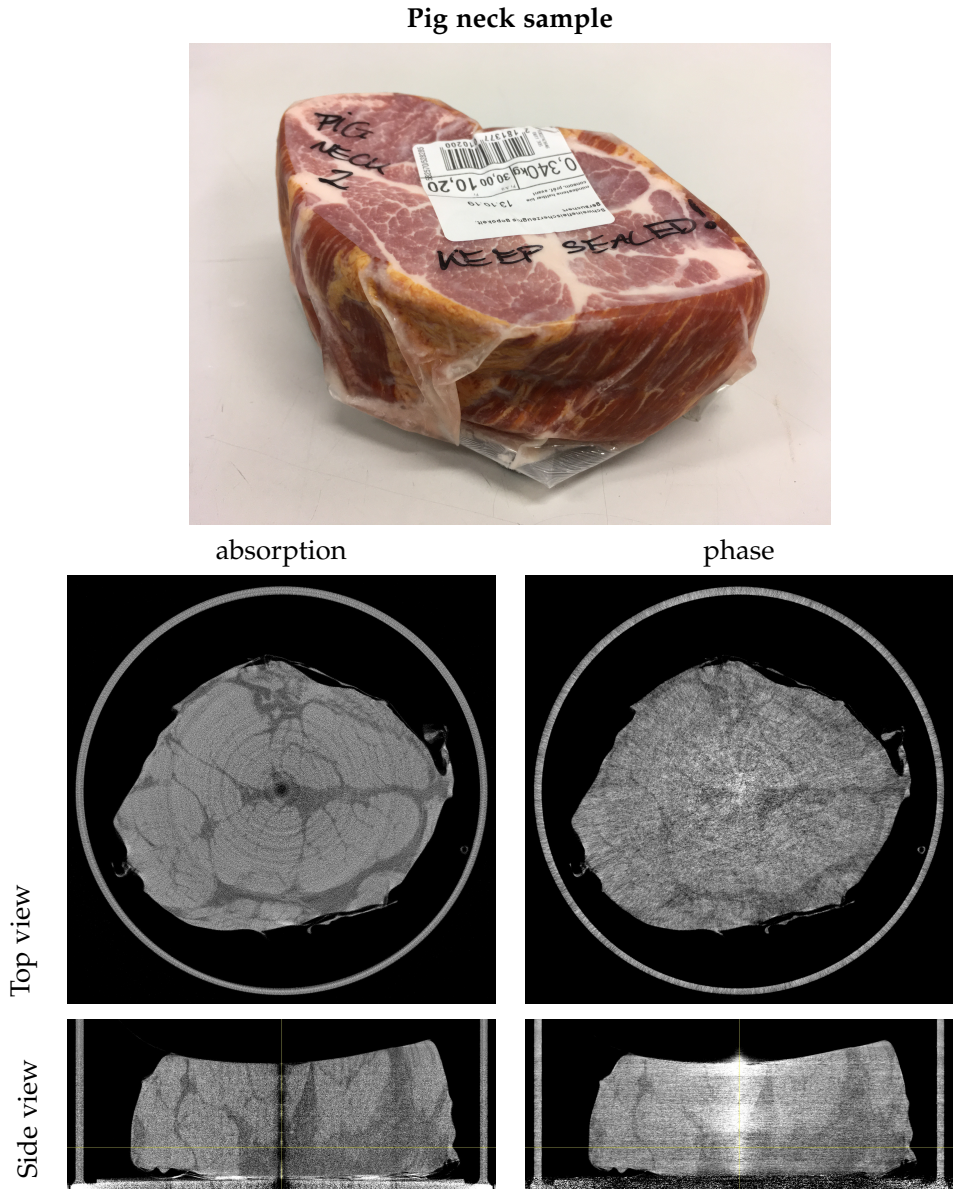

Figure 2.4: Results of a tomography scan of the shown pig neck sample. On the left side the absorption channel is shown while on the right hand side the phase channel is shown, in top and side view.

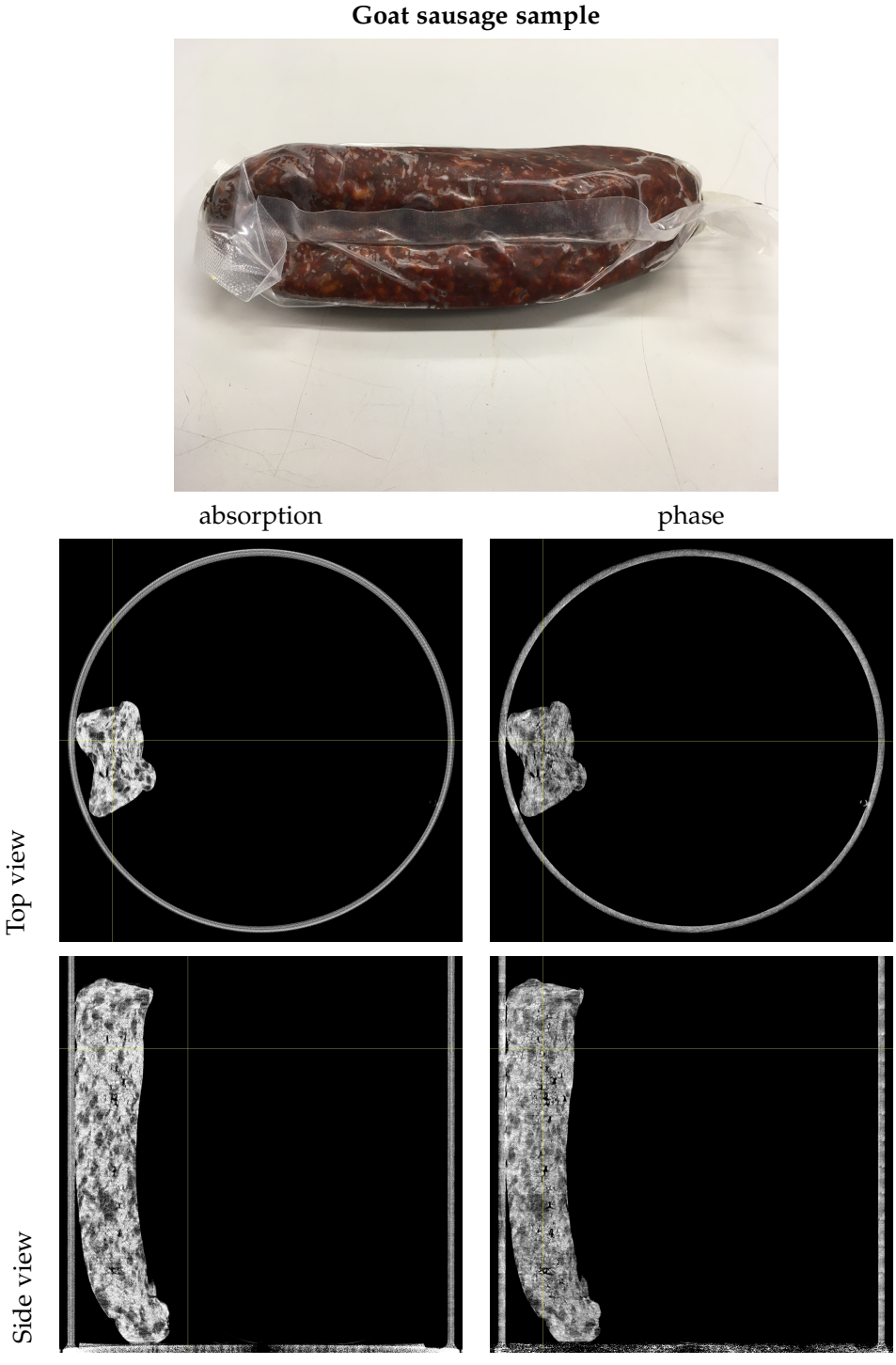

Figure 2.5: Results of a tomography scan of the shown goat sausage sample. On the left side the absorption channel is shown while on the right hand side the phase channel is shown, in top and side view.

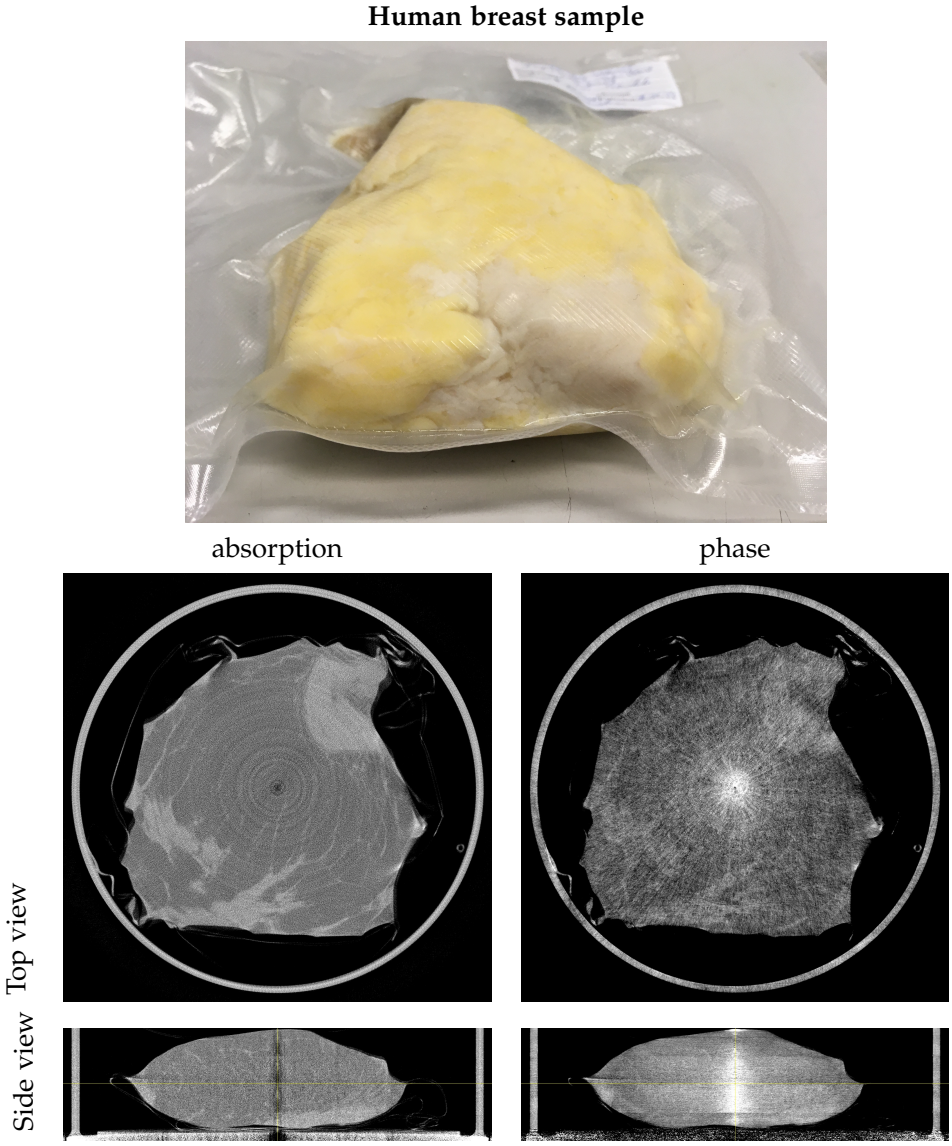

Figure 2.6: Results of a tomography scan of the shown human breast sample. On the left side the absorption channel is shown while on the right hand side the phase channel is shown, in top and side view.

Chapter 3

Phase Drift

The flat-field correction, as introduced in section 2.3, assumes that the flat-field is static. Since it is only possible to either measure a sample or the flat-field, this approach assumes a sufficiently static flat-field. The arising issue is that the flat-field correction is with the equations 2.1, 2.2 and 2.3 inaccurate. To investigate the temporal behaviour the flat-field can be measured at different times and then subtracted from each other to obtain the temporal change of the parameters as shown in fig. 3.1.

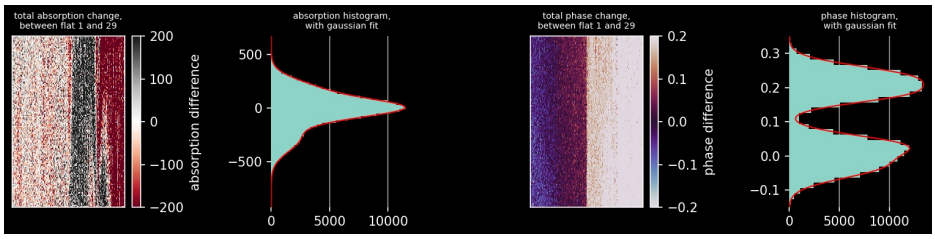

Figure 3.1: A comparison between two flats taken half an hour from each other in absorption on the left-hand side and the phase on the right-hand side. As the image shows the flat changes considerably over time and a static flat correction would lead to large errors. The difference of the two flats shows obvious regions which resemble the gratings perfectly. The large difference has the spatial resemblence of the phase grating while each half is again split into two matching the analyser g2 gratings. It can be seen that different parts of the detector seem to drift differently where the drift is almost homogeneous over the single grating regions.

For a random phase drift for each pixel (uncorrelated), the expected phase map of the difference of two flats should result in a Gaussian value distribution on the histogram. Figure 3.1 has the interesting property that the phase

drift somehow causes the histogram to bifurcate. The absorption difference shows on the left side what would be expected, a random deviation from the mean value at each pixel while the right side the shift is correlated in a red and black region. Taking a closer look, the data can be split in half or quarters, coinciding with the areas covered by individual parts of the g2 grating, to see if the distribution of the pixel values resembles a Gaussian again.

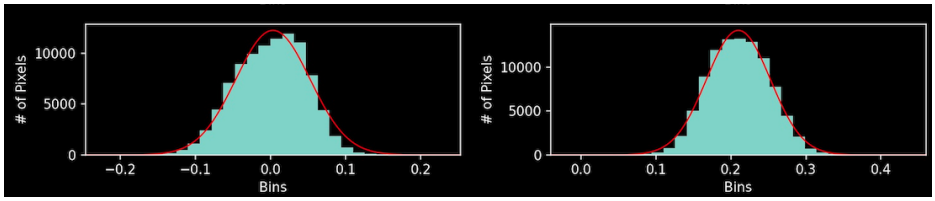

Figure 3.2: The same phase difference as in figure 3.1 but each side separately fitted. On the right side it is obvious that this does not represent a Gaussian well yet.

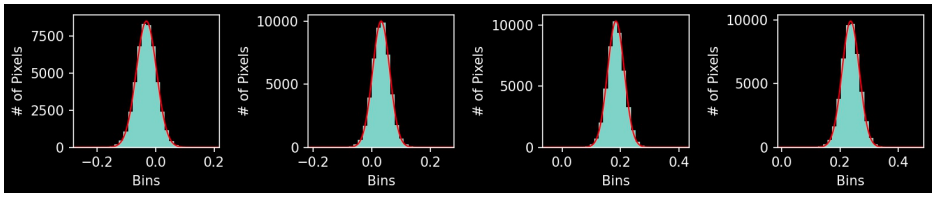

Figure 3.3: The same phase difference as in figure 3.1 but each grating separately fitted. For each grating a Gaussian fit represents the histogram a lot better.

This effect occurs for every measurement with varying intensity and direction of the shift. From this the conclusion can be made that different parts of the detector drift at different rates. For the following analysis the focus will be only on the phase channel as it is by far the most sensitive to this effect and the goal of this work was to enhance..
The purpose of this phase drift analysis is to find a confidence time interval such that flats are only taken when it is necessary and therefore save acquisition time. Taking a flat requires the sample to be removed out of the beam and put back to where the tomography is resumed. This can take a considerable amount of time for large samples.

The phase drift consists of a short time scale variation, which is mostly random, and uncorrelated and a long scale drift which shifting the mean

value of the phase towards a different value in an almost linear fashion as can be seen in figure 3.4.

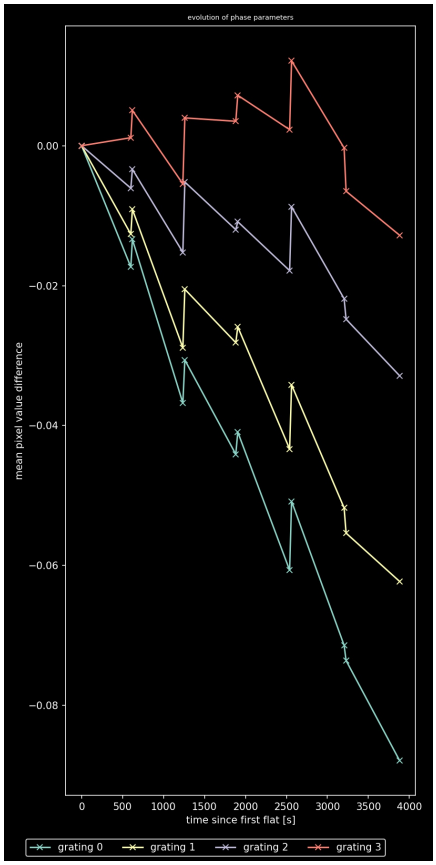

(a) Long term variability of the histogram mean value of flat-field measurements.

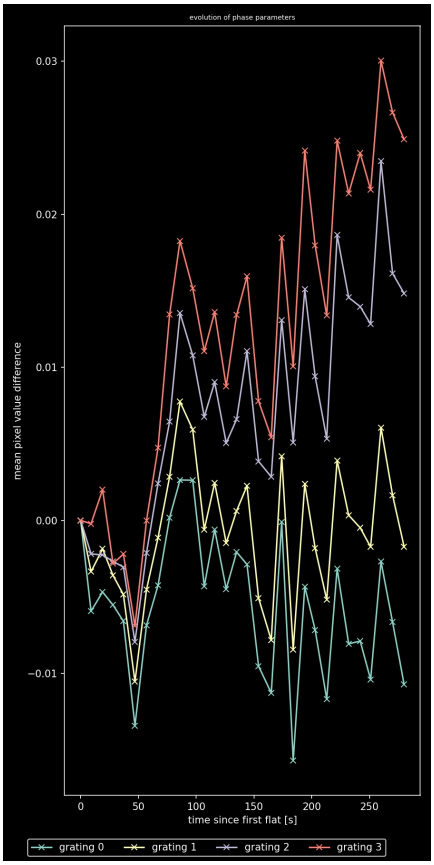

(b) Short term variability of the histogram mean value of flat-field measurements.

Figure 3.4: The variability of the flat-field is more or less linear over longer regions with slope changes along the way, while the short term variability is chaotic but the overall trend of the long term variability slope. Grating 0 defines the grating plate of g2 to the very left and grating 3 is the one to the very right.

In figure 3.4a it is visible how often a flat is taken and how much acquisition time is due to those. Therefore it is of interest to reduce the number of flats taken. Since the data come from a normal tomography routine described in section 2.2 a single segment takes nine minutes to measure while the second and third flat are only taken at around eleven minutes. This around two

minute difference comes from the time the vertical motor takes to move the sample out of the beam and back into it again.
It is, however, not possible to get information about the flat-field while performing a tomography measurement and therefore a change in linear slope can not be detected. To find temporal intervals in which a linear approximation is suitable, tomography data have been reconstructed by reducing the number of flats used. This will be the topic of the next section.

3.1 Residue Analysis

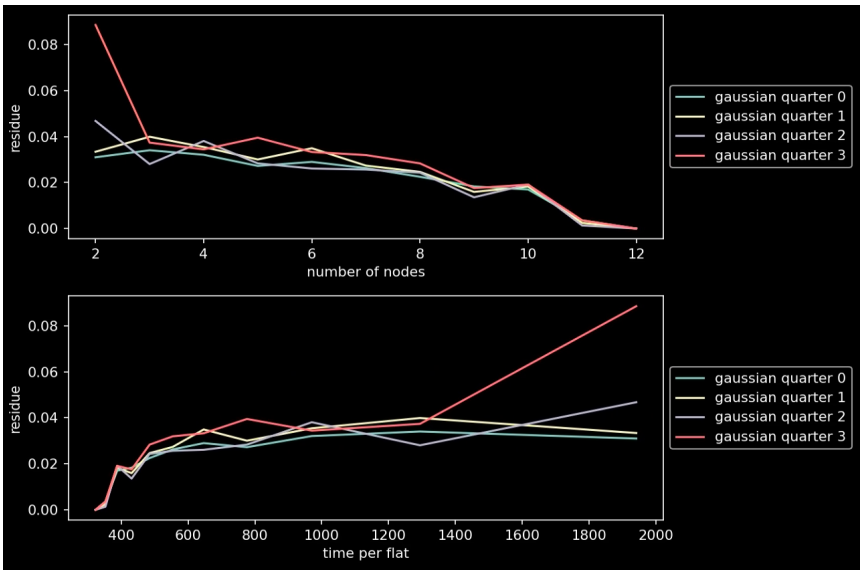

Figure 3.5: The evolution of the phase mean value for all gratings. On the top the difference between the original data set and the interpolated one is plotted against the number of flats used (flats correspond to nodes). On the bottom the residuals are plotted over flat frequency (total tomography time divided by amount of flats used).

As flats take a lot of time to be obtained during a tomography the goal was to find a time scale for which the flat can be approximated to be linear. For that purpose a residue analysis was done. This means for a tomography measurement first the flats were compared by systematically leaving out flats and interpolating between the ones that are left over. The interpolation was then compared to the full dataset and the error to it was calculated. Afterwards the tomography was flat-field corrected by these flat configurations to see how the residue translates to reconstruction quality. This should

then tell what equidistant time intervals can be described as a piece-wise linear function.
For the analysis the time intervals of the tomography needed to be split up. The first interval would be the first and last flat with linear interpolation between them. Then, in the next step, the flat which was closest to the mathematical middle of the interval was picked and the linear interpolation was done between the first and second and the second and third picked flats. This pattern was continued until all flats were used. The results were then fitted by piece-wise linear functions and compared to the original data analysis, which used every flat.

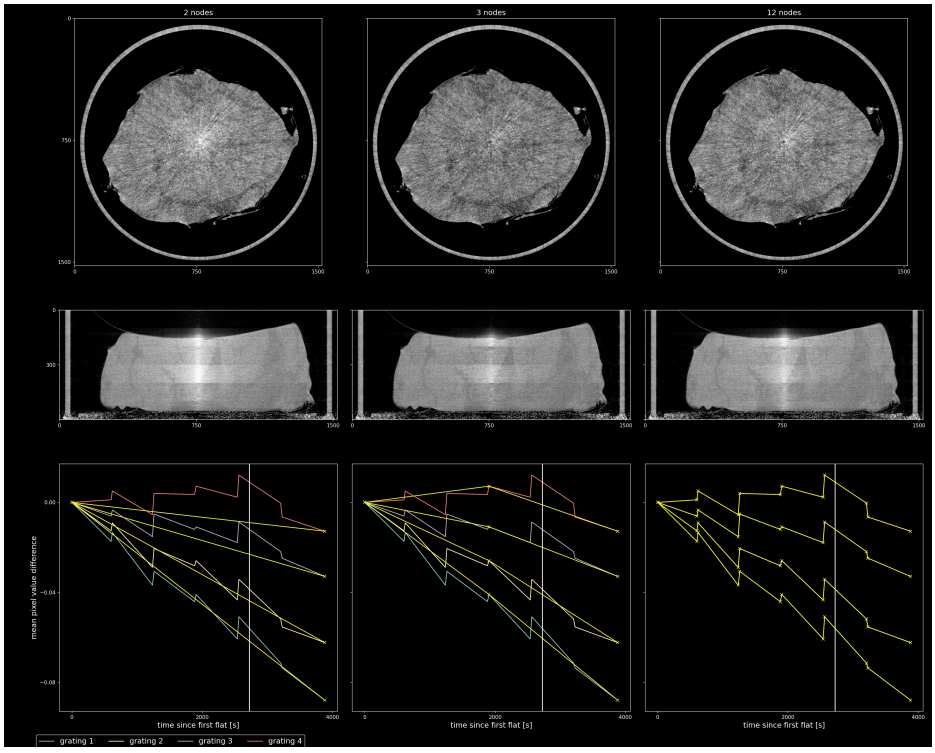

Figure 3.6: Reconstruction of the pig neck sample with different flat configurations. Columns correspond to the same analysis, where the top row images are the top views, the middle row images are the side views and on the bottom are the average values of the DPC projections for the areas correponding to the four parts of the g2 grating. as well as the used flats with the interpolation between them (in yellow). A vertical line indicates from which measurement cycle the top view image is taken.

We define a node to be a flat which was closest to a interval point and serves as a intermediate point for the linear interpolation. The flats were not distributed evenly over time since there were always two flats done at once in between the slices. In figure 3.5 the strongest decline in error happens for the change from two to three nodes (mostly due to the right half of the detector), while from there on the residuum slowly decreases. Changing the node axis to time per flat shows that the residuum has a plateau from 600 to 1300 seconds (10-22 minutes).
To match the residuals to data quality, the flat-field curve for each residual was used to correct the tomography. The flat residue analysis and reconstruction agree that going from two flats to three has the biggest impact on the error as well on the reconstruction. What is surprising is that afterwards the reconstruction does not get better by using more flats but worse. The rotation center artefact gets brighter again for more nodes as it can be seen in figure 3.6. The two-node case indicates that much time can be spared by taking the flat measurement less often with little impact on the data quality. The three-node case shows a definite improvement at a little time cost (2 minutes).

3.2 Ideal Flat Correction

The results from figure 3.6 do not match the assumption that this method would result in more artefacts the less flats are used. They enhanced the reconstructed image which was not expected at all. There are several possible explanations as cutting away very high flat values (on the right two graphs in figure 3.4a) might help the flat-field correction to account for the long term drift while not picking up on the short term variability. This supports the claim of the existence of a chaotic and random short term variability or a slight displacement of the sample during the measurement induced by the movement of the sample holder as well as a correctable long term linear slope. Therefore, the short term variability might influence the measurements in an accessible way. To put this knowledge better to use the flat-field correction algorithm had been adapted to linearly interpolate between the flats instead of using only the mean value of the two. To improve this correction in section 5 a different flat correction function will be introduced.

In order to deepen the understanding and to find proof of those claims a simulation of the data acquisition should bring insight of what caused the bright spot in 3.4a to almost vanish and ideally remove this artefact as a whole.

Chapter 4

Simulation

The goal of the simulation is to find the origin of the artefacts visible in the reconstruction. If an artefact can be reproduced and controlled by a parameter this will help to understand the underlying cause and find a solution to correct it in the real data.

4.1 Model

For the simulation of the data the Python packages ASTRA [20, 21] and TomoPy [23, 24] were used. The source, the phantom, as well as the reconstruction, were based on functions from these libraries with the geometry adjusted to represent the GI-BCT system. The simulation consists of three major parts: the phantom modelling, the tomography simulation and the signal analysis. Simulation of tomographic imaging of a phantom yields sinograms of the absorption and refraction, which serve as the reference solution. Then, to ensure the results look similar to real data and possibly even containing some intrinsic properties of the gantry system itself, a time series of real flat-field measurements are loaded and interpolated in between to obtain a temporal change of the background that resembles features found in section 3.

The underlying model which is used to calculate the phase curve was introduced in equation 1.7.

4.1.1 Phantom

For the simulation the SheppLogan3D phantom was loaded with the ASTRA package in a size such that most of the interesting features of the phantom would fit in the wide but slim virtual detector (which was chosen to match the size of the real detector of 25x300 mm) without the need to stitch together multiple measurements on the vertical axis. The size was then fixed to 256^3

voxels divided by the binning. The top and side view of the phantom is shown in figure 4.1.

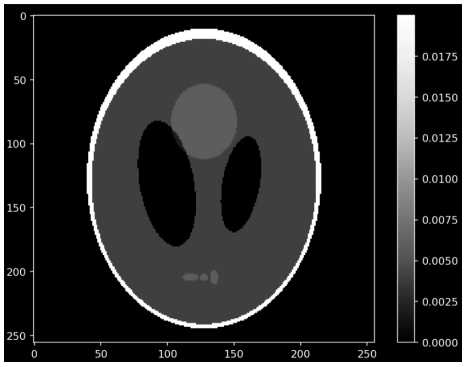

(a) Top view of phantom.

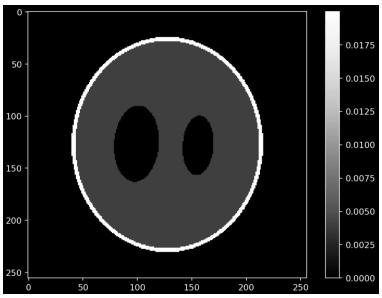

(b) Side view of phantom.

Figure 4.1: Ground truth for the Shepplogan3D phantom.

4.1.2 Attenuation and Refraction

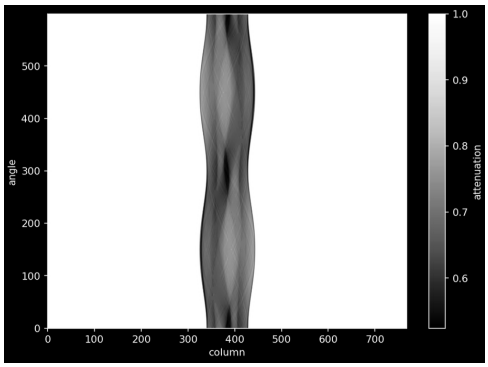

(a) Sinogram of the attenuation.

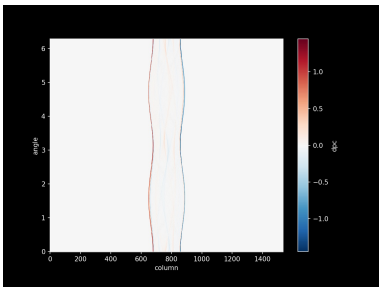

(b) Sinogram of the refraction.

Figure 4.2: The physical properties of the phantom imaged from all angles. The attenuation sinogram defines how much of the input will be decreased while the refraction will define how much the input is refracted by the phantom for every angle and pixel.

The sinograms of the phantom were obtained with the ASTRA toolbox and were then used as values for attenuation (by using the Beer Lambert law described in section 1.2) and the refraction, which was calculated as the horizontal derivative. The obtained sinograms for attenuation and refraction can be seen in figure 4.2 and are created with 600 angles per rotation, which

was the same angular distribution used for tomographies up to this point in time.

4.1.3 Flats

Flats are necessary to obtain the change of the signal out of the measured sample data. A flat includes the combined effect of the inhomogeneity of the source and the gratings themselves, as well as the interferometric Moiré fringe. It can be used in the simulation to obtain similar results with idealised circumstances and full control over all other system properties. This should enable the results to look similar to the real data, but with the ability to systematically control the parameters which are not accessible in reality. If flats are used just as a background image, it can be corrected perfectly with a flat-field correction. The correction does not cause any artefacts, which shows that using a real data flat as an illumination does work as intended without unwanted effects. Even using different flats for correction can be corrected by the difference of these two flats as one would expect. If it is assumed that the flat is not known which is true for reality, the image can still be corrected as it is a static linear problem.

4.1.4 Temporal Evolution

To simulate a phase drift the inclusion of real flats allows to use a realistic phase drift (even though it will be linearly interpolated) instead of an artificial one. It is not yet fully understood what causes the drift nor how it should behave. The only assumption put in place is that flats have a linear change on large scales, as it was indicated by data in section 3.1. Therefore, the flats have been interpolated linearly and its parameters are then plugged into the phase stepping model for the simulation. The speed of temporal change is defined by how many points between flats are interpolated (e. g. plugged into the model to calculate the projections with).

To simulate a tomography a total of 3000 points are needed as we have defined the number of angles to be 600 and the amount of phase steps used is five. As for a tomography all angles are measured for a single phase step before moving on, the drift will impact one measurement as it would for a tomography (the drift amount is defined by the interpolation).

The flat-field correction can then be done in different ways. To ensure internal consistency of the technique, when correcting with the interpolated background flats, the results should become artefact free. The used correction for the following results is chosen to be done the same way as it was for the original data (using the mean of the flats before and after).

The results of those temporal simulations can be found in figures 4.3 and 4.5.

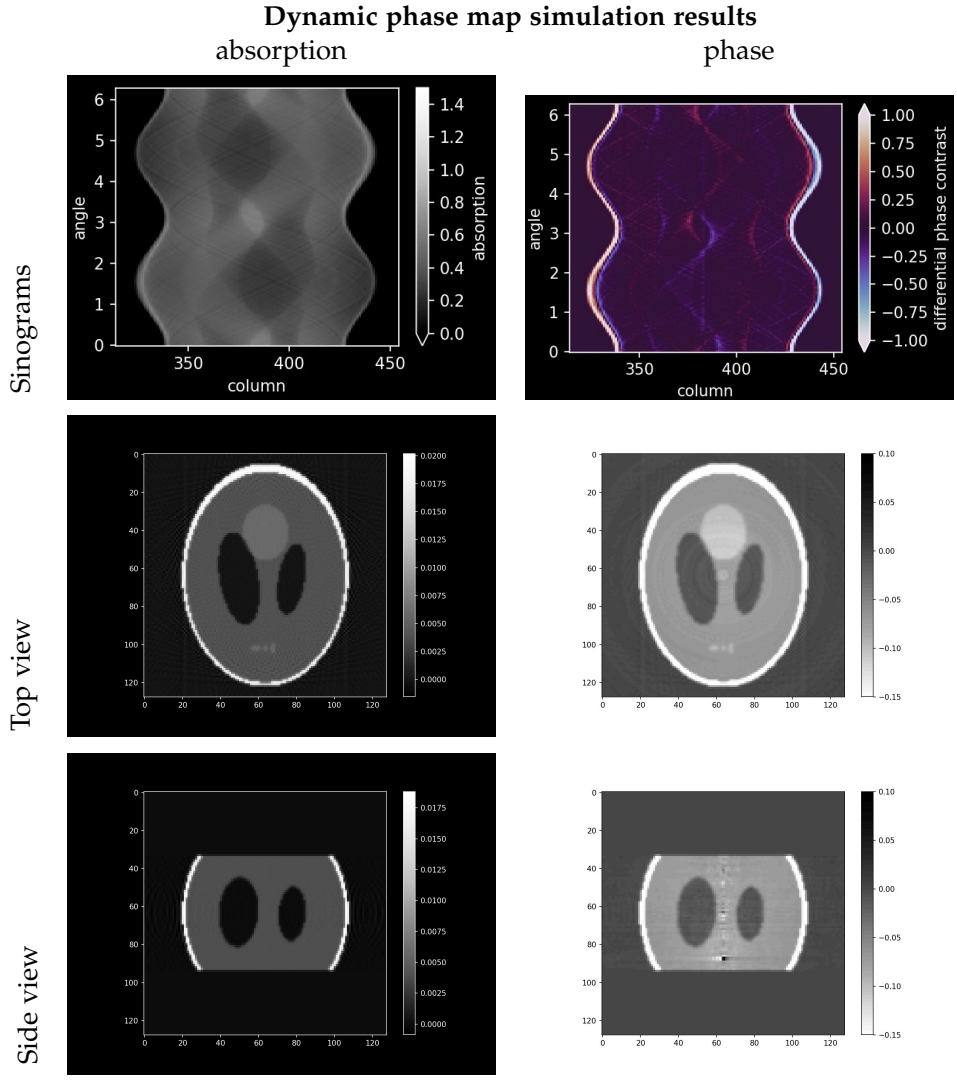

Figure 4.3: The results of the dynamic phase map simulation of a tomography. The absorption image looks like a perfect reconstruction while the phase image has ring like artefacts as well as random shifts on the rotation center.

The figures in figure 4.3 show that the phase reconstruction is more sensitive to deviations than the absorption channel. This is to be expected since these fluctuations from the correction will be logarithmically suppressed while the phase has a linear dependency causing errors or shifts to have a lot of impact. The horizontal slice of the phase contrast has ring artefacts, which the absorption does not have and in the side view the rotation centre of the phase image exhibits small bright and dark error regions, which come from the imperfect flat correction. Therefore, having a uncorrected phase drift in the tomography should not cause a bright spot but a rotation center with a lot of value fluctuations. The ring artefacts are located at points where the sinogram of that slice has vertical artefacts over the whole angle range of which some can be seen on the phase sinogram on the top right in figure 4.3 but these shifts are in general to small to see by eye. For real data these vertical artefacts on the sinograms are more pronounced as visible on figure 4.4.

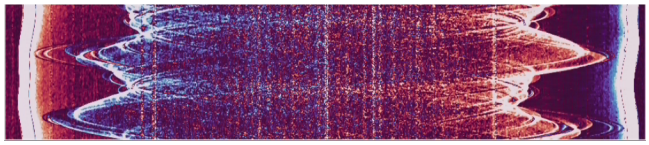

Figure 4.4: Sinogram of a measurement with vertical artefacts visible by eye.

This acquisition scheme can be inverted to a different but similar procedure, where for each angle all phase steps are measured before moving to the next angle. The results to this simulation look similar at first, but are almost artefact free for the phase when performing a interpolated correction where this does not work for the case of the normal acquisition (see figure 4.5). Also, when using more and more of the flats to correct the data with, the case of the immediate phase measurement benefits the data where the other does not in the same manner. An additional advantage of the inverted acquisition scheme is that the flat-field correction can be applied on a linear interpolation between the two flats from before and after the tomography and be corrected at many points in time, while the original one has to be corrected with the mean value as the signal retrieval algorithm does only allow a single phase map to be used for correction for all 5 phase steps. Since these phase steps are temporally far away from each other this correction will be limited by the phase drift between these images where the inverted scheme does not have that. The better performance by the correction comes partially from the linear flat interpolation between the real flats which was expected to work better with this different acquisition method. It indicates, however, that the measurement benefits from a short acquisition time as the drift between the single measurements for one angle decreases and results in a smaller error for the signal retrieval.

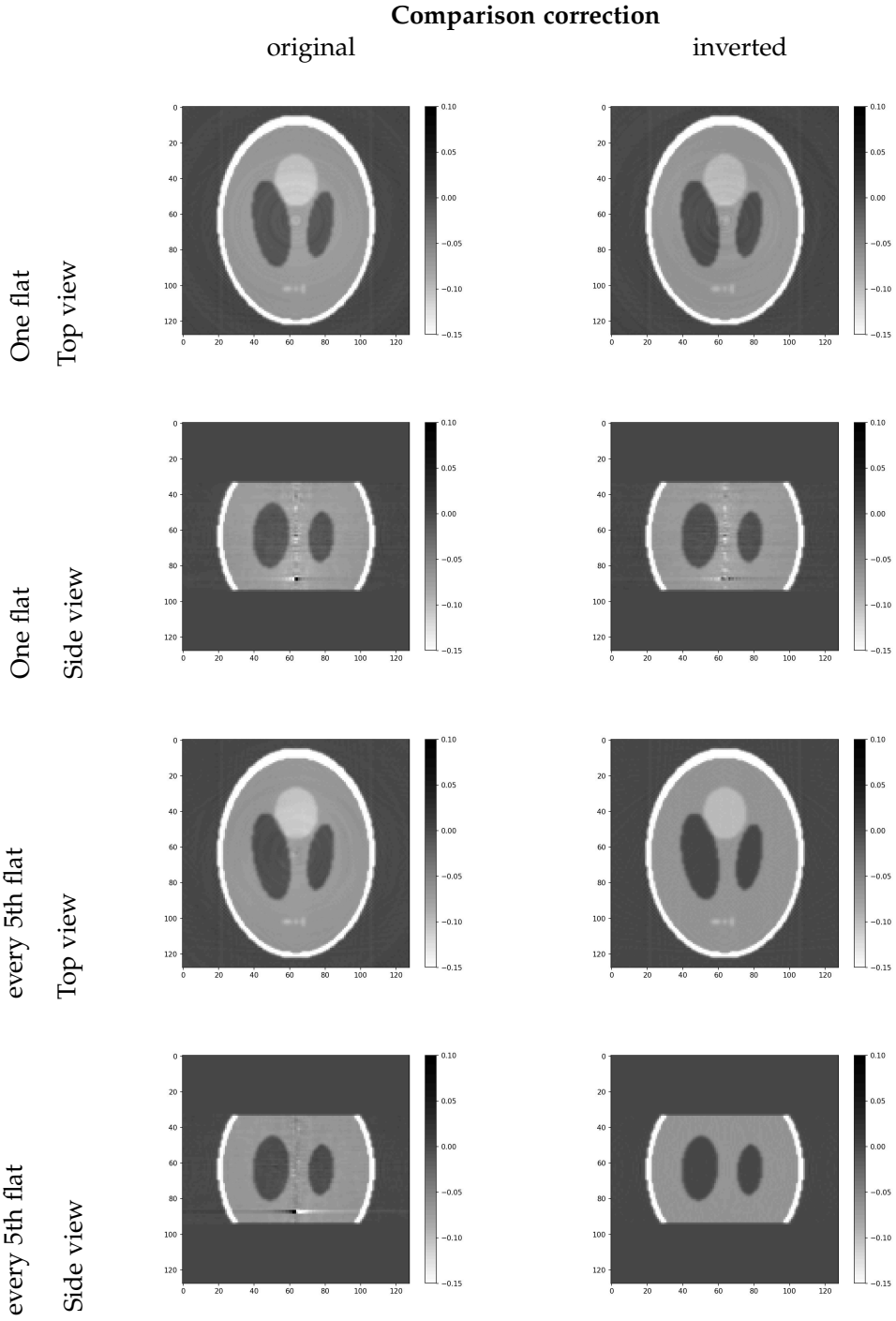

Figure 4.5: Comparison in flat correctability between the acquisition routine measuring every angle before doing a phase step (”original”) and the ”inverted” routine where all phase information is collected before moving to the next angle. The correction ”every fifth flat” means that instead of using the average of the flat before and after the measurement, every fifth flat from the interpolated series is used to correct the drift directly.

4.1.5 Period Mismatch

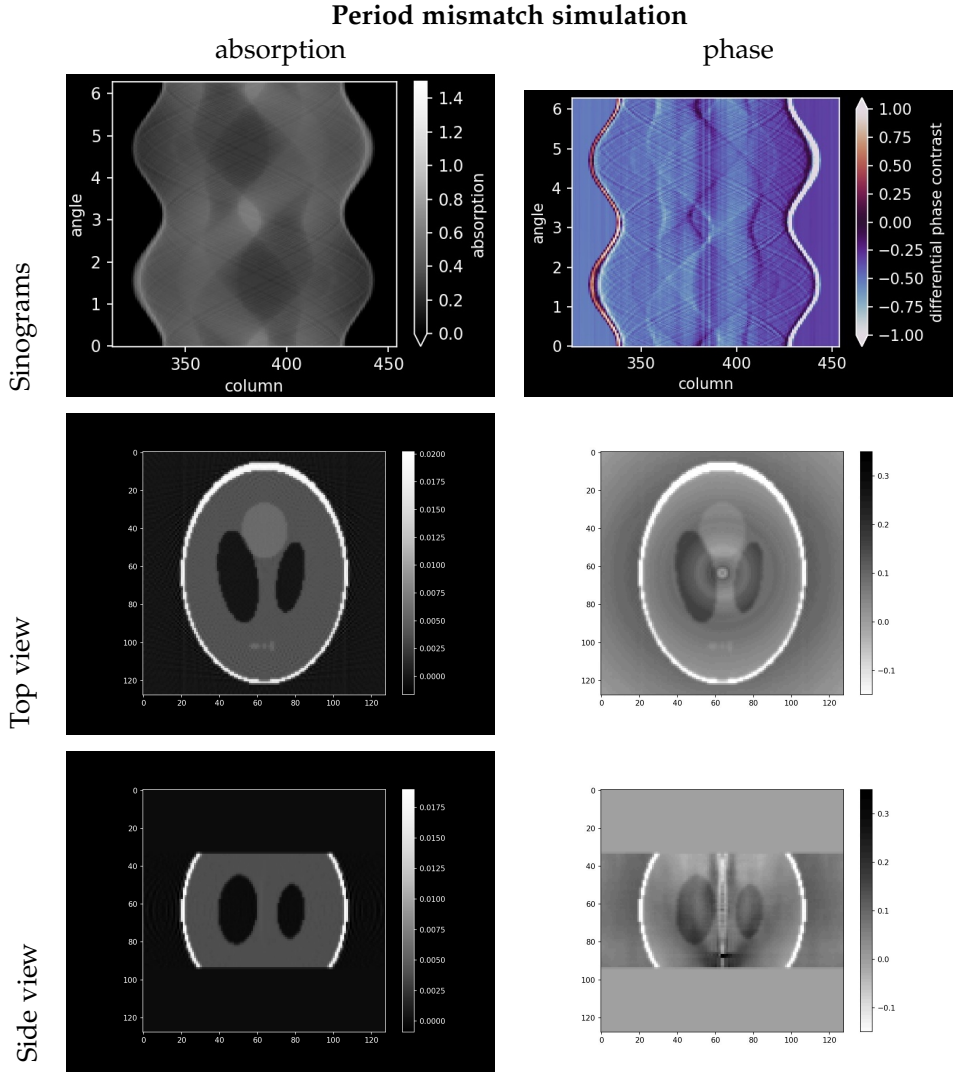

Figure 4.6: The results of a period mismatch simulation. For the channel already in the sinogram a phase difference between the left and right side of the image is visible which is not the case for the simulations before. The ring like artefacts have radially a more smooth profile instead of being like singular circles for the tomography simulation in figure 4.3. On the side view of the phase a triangular shape as well as a overpowering artefact in the rotation centre are visible.

For real measurements, the period of the phase curve is not always the very same when fitted and varies slightly each measurement. To investigate what effect a phase mismatch can have on the reconstruction, the tomography has been also performed by measuring a wrong phase range of g0. The simulated data were then analysed assuming a wrong period. The results of this simulation can be seen in figure 4.6.

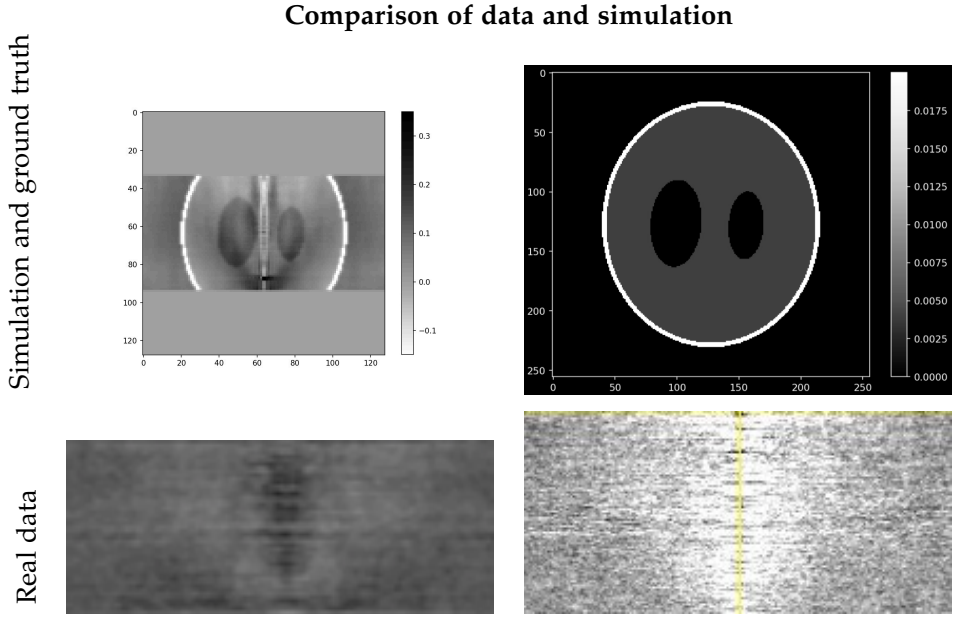

Figure 4.7: The results of a phase mismatch simulation. For the channel already in the sinogram a phase difference between the left and right side of the image is visible which is not the case for the simulations before. The ring like artefacts have radially a more smooth profile instead of being like singular circles for the tomography simulation in figure 4.3. On the side view of the phase a triangular shape as well as a overpowering artefact in the rotation centre are visible.

The sinogram of the phase channel on the top right corner of figure 4.6 shows an interesting feature: it has a non-zero phase as a background and the value shifts from the left to the right side of the phantom. The reconstructions do show a central artefact which consists of a central region and a cone like shadow with the tip at the bottom. This type of artefact can indeed be found in real data reconstruction, indicating that a phase mismatch must be present. The period had been remeasured. It turned out that indeed the period was off and it needed to be adjusted from 0.003474 mm to about 0.00408 mm which is 15 percent larger (almost the same mismatch as in the simulation).

4.2 Improvements

The results of the simulation were able to connect artefact to cause which could be corrected for the real data. First, the simulation gives no evidence that the bright spot is caused by a linear phase drift and can therefore not be corrected at this point in time if it stems from the short term variability. The second claim from the simulation is that the phase curve acquisition should be done as quickly as possible since the signal retrieval and flat correction benefit from shorter times between the phase measurements of the same projection angle. The third important realisation was that the system was tuned to a wrong period which caused central artefacts.
The data acquisition and analysis will be adjusted to these insights in the following chapters by changing the signal retrieval to enable any correction to take place directly in this algorithm (in section 5). With this change the signal retrieval would be able to correct phase drifts in a single phase step measurement if it is provided with good phase drift parameters. Good parameters are hard to predict but one possible option is to use the pixels to the side of the sample to give an estimate on the parameter drift on the whole image. To do so the phase stepping routine would need to be changed into a constant movement, which has not been explored to this point. To gain an additional parameter for the image acquisition this idea will be investigated in chapter 7.
The tomography acquisition procedure will be adjusted to use less overall time in chapter 6 to check if this insight holds for real measurements as well.

Chapter 5

Signal Retrieval

This chapter will focus on improving the data quality by combining signal retrieval and flat-field correction. In chapter 3, the temporal variability shown in figure 3.4 was introduced. Flat correction for the phase channel to this point was the subtraction of a single phase map. If a linear drift causes artefacts in the reconstruction, this method will correct them through interpolation. It can in general correct for any drift for every single pixel. Often this information is unknown and some form of model or interpolation has to be used.

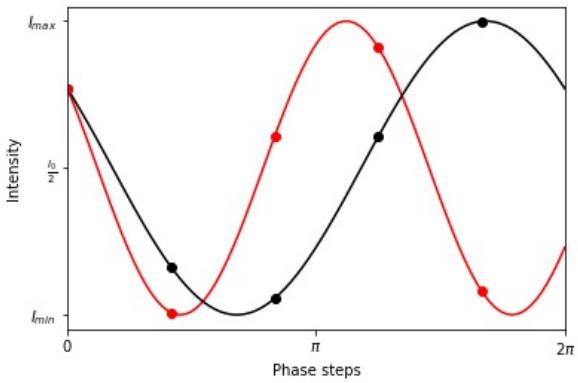

Figure 5.1: Two phase stepping curves. The difference between the two is a linear phase shift of the form $\varphi = (1 + a)\varphi_0$ where a is a scalar and φ_0 is the position of the piezo. Therefore, curves $\sin(\varphi)$ with different scalars a will result in a sine with a different period.

If a linear phase drift is present in the data the measured curve for a single pixel and a single angle would look like a sine with a different periodicity, as it is shown in figure 5.1. Therefore, correcting a linear drift by just adapting the period the absorption and visibility would be correct. The phase value would shift over the angles as the starting point in figure 5.1 would move due to a uncorrected phase change which in turn changes the phase parameter of the data.

Up to this point signal retrieval was done by fast Fourier transform, where the coefficients were used to calculate the absorption, phase and visibility. The same result can also be obtained with a least square fit of the linear matrix equation of the type $X \times M = Y$, where Y are the measured data, X is the matrix of parameters to fit and M will be the amplitudes of the parameters of X. One parametrisation for this problem can be chosen as:

$$\begin{bmatrix} \sin(\varphi_0) & \cos(\varphi_0) & 1 \\ \sin(\varphi_1) & \cos(\varphi_1) & 1 \\ \sin(\varphi_2) & \cos(\varphi_2) & 1 \\ \sin(\varphi_3) & \cos(\varphi_3) & 1 \\ \sin(\varphi_4) & \cos(\varphi_4) & 1 \\ ... & ... & ... \end{bmatrix} \cdot \begin{bmatrix} x^0 & x^1 & ... & x^{n-1} \\ y^0 & y^1 & ... & y^{n-1} \\ r^0 & r^1 & ... & r^{n-1} \end{bmatrix} = \begin{bmatrix} P_0^0 & P_0^1 & ... & P_0^{n-1} \\ P_1^0 & P_1^1 & ... & P_1^{n-1} \\ P_2^0 & P_2^1 & ... & P_2^{n-1} \\ P_3^0 & P_3^1 & ... & P_3^{n-1} \\ P_4^0 & P_4^1 & ... & P_4^{n-1} \\ ... & ... & ... & ... \end{bmatrix} \tag{5.1}$$

In this equation r^i corresponds to the absorption, x^i and y^i are the fitting parameters of the periodic part of the phase stepping curve. By fitting then:

$$P_j^i = r^i + x^i \sin(\varphi_j) + y^i \cos(\varphi_j) \quad \forall\, j \in [0, 1, ..., k-1],$$

for k phase steps where the upper index stands for the pixels P^i (the 2D projections are transformed into a long row) and the lower for the phase steps. Therefore each set of x^i, y^i, r^i will describe the a curve like equation 1.7. The parameters can then be recovered as shown in equation 5.2 where Λ is the absorption, φ the phase and χ the visibility.

$$\begin{aligned} \Lambda^i &= r^i \\ \varphi^i &= \arctan\left(\frac{y^i}{x^i}\right) \\ \chi^i &= \sqrt{x^{i2} + y^{i2}} \end{aligned} \tag{5.2}$$

The full matrix equation $X \times M = Y$ has then the form shown in equation 5.1 and can fit the whole image at once with a single least square fit. This equation uses the same matrix X for all data of a single slice. To adapt this

to have for each single pixel of each projection a separate correction, the dimensions of the matrices will increase to large block diagonal matrices as it is shown in figure 5.2.

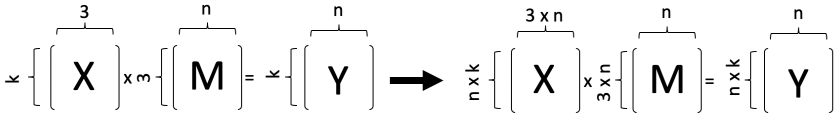

Figure 5.2: Dimension change of the matrix equation $X \times M = Y$ where n is the number of pixels and k the number of phase steps.

The left-hand side of this equation consists of sparse matrices, causing a lot of unnecessary operations in a least square fit. This results in an unreasonable computation time as python can not parallelise this operation automatically. For this purpose the programming language julia was used to do the calculation pixel-wise. This way also the memory usage of the computer can be reduced. This equation has instead of k (k phase steps) now $k \cdot n$ (n is the number of pixels of the detector) initial parameters per signal retrieved projection, as each pixel has its own drift correction. Even though this process can use multiple CPU cores it is still by at least a factor three slower than the straight linear fit for six cores instead of one.

Results of this technique can be seen in figure 5.3. They show the comparison of the signal retrieval with and without period correction and linear phase drift interpolation between the flats (only for the new signal retrieval). From the figure it is visible that correcting the phase mismatch does reduce the central bright artefact as well as its surroundings (the cone around the center in the simulation). The new signal retrieval is even darker and more uniform in brightness throughout the image. The value range for the new signal retrieval has to be chosen larger as the signal sinograms feature larger values for all analyses performed. The period mismatch corrected signal retrievals however both show a ring artefact (red arrow in figure 5.3) at the location of the grating gaps in g2. By correcting the period mismatch there will quickly appear the patterns found in the simulation (figure 4.6) if the value is off.

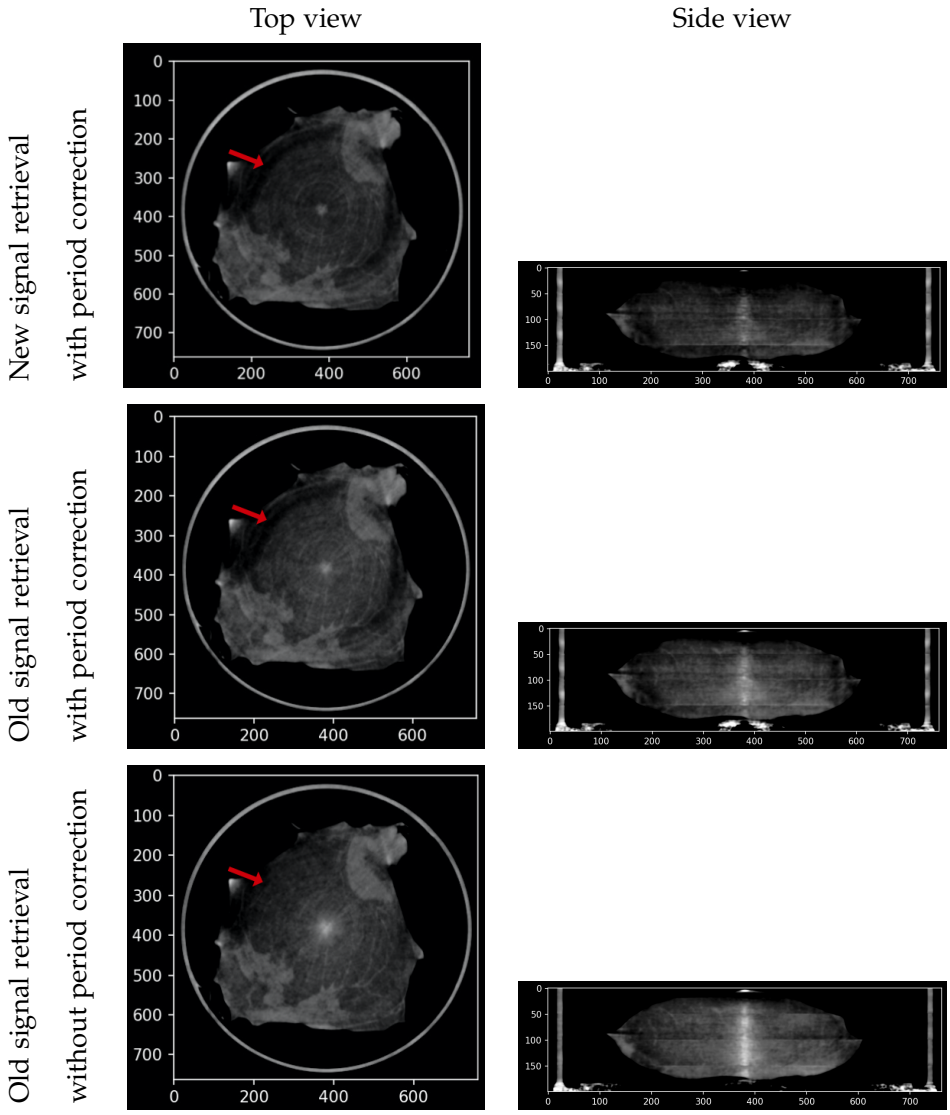

Figure 5.3: This figure contains images of the top and side view of the human breast sample. The left side has the top view and the right side shows the cross section through the rotation centre. The samples images from top to bottom seem to brighten up towards the middle which is visible on the top and side view. On the top view the red arrow points to the induced ring artefacts by the period correction and new signal retrieval.

5.1 Further Improvements

As can be seen on Fig. 3.4b a linear interpolation is not a perfect representation of the phase drift as it has random shifts on small time scales and behaves piece-wise linearly over long periods of time. The measurement routine is set up to do phase stepping only every two rotations. The phase parameter can therefore not be calculated out of the data. For this reason it is of interest to have the option to monitor the phase drift continuously during the tomography. To do so the data acquisition routine needs to be changed such, that the phase stepping is more frequent than only every 4π by continuous g0 movement, maybe even every frame or continuously. With that it should improve this signal retrieval to account for small scale variability. The phase factor can be calculated out of the 20 pixel wide edges of the image and scaled over the whole image by scaling in between the flats. If this works well it could replace all flats except for one in the beginning and one at the end and save a lot of acquisition time. This points towards investigating a continuous g0 movement during measurement which will be investigated in chapter 7.

Chapter 6

Adapted Acquisition

The results of section 4.1.4 indicated that decreasing the phase acquisition time could improve the flat correction and therefore the reconstructed image quality. This chapter will discuss how the acquisition script was changed and how the results compare to the measurements of section 2.4 and chapter 5.

6.1 Acquisition Script Changes

To decrease the acquisition time of the phase stepping curve, the measurement was split into multiple measurements of a phase stepping curve of fewer sampling points. Thereby the whole phase information is acquired in a shorter amount of time as fewer rotations are needed. In addition the rotation speed of the sample holder was increased to reduce the time it takes to measure the phase stepping curve even further. The phase stepping of the script was changed as well to measure and rotate continuously instead of stopping the rotation, do a phase step and start again afterwards. This change will cause the projection angles to not be measured at the same point in time as before since the measurement of each subsequent phase step starts one rotation and one second later (waiting for the piezo to reach its commanded position).
The applied changes to the acquisition script are listed below in table 6.1 and the new acquisition scheme is sketched in figure 6.1. Compared to the former acquisition scheme (see section 2.3), the adapted acquisition script measures the full phase stepping curve in one minute and two seconds compared to nine minutes before. Since the adapted script acquires frames continuously during phase stepping, the total exposure of the adapted acquisition script will be almost 4 minutes shorter than for the former script (as we wait for one second for the piezo to reach its destination without a full rotation). In addition the angular resolution increased by reducing

the angular step-size from 0.6° to 0.36°. Here we define the multiplicity to be the amount of times the same measurement is performed. These measurements will be signal retrieved together to match the statistics of higher exposure time measurements and make them comparable. To that end, the measurement was done with a multiplicity of five.

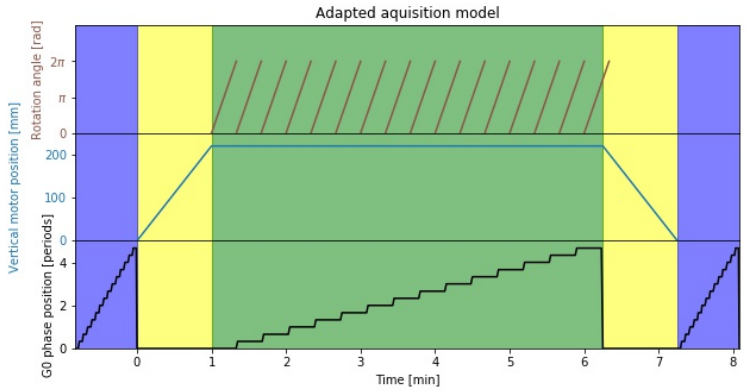

Figure 6.1: A sketch of the acquisition routine of the adapted tomography script with the mentioned parameters of table 6.1 illustrated. The top row shows the motion curve of the sample rotation motor. The middle curve corresponds to the vertical sample motor which puts the sample in and out of the photon beam and the bottom row shows the g0 movement of the phase stepping. The x-ray source is always on. The blue regions correspond to flat measurements, in yellow are regions where no images are acquired and green illustrates where the detector acquires images. A measurement of a 12.5 mm-high fragment of the sample will therefore take around nine minutes (depending on the vertical location of the slice). The exposure time of the tissue is 5.23 minutes and only five minutes are used as data and 14 seconds is waiting during phase stepping. Therefore the measurement will take over 15 rotations. Note that the flat measurements also take now 50 seconds each.

Rotations per minute:	1	→	3
Phase steps:	5	→	3
Angles:	600	→	1000
Frame rate:	10 Hz	→	50 Hz
Multiplicity:	1	→	5

Table 6.1: Parameters that were changed from the original acquisition script to the new one. Multiplicity in this listing refers to the amount of times a single tomography measurement is done.

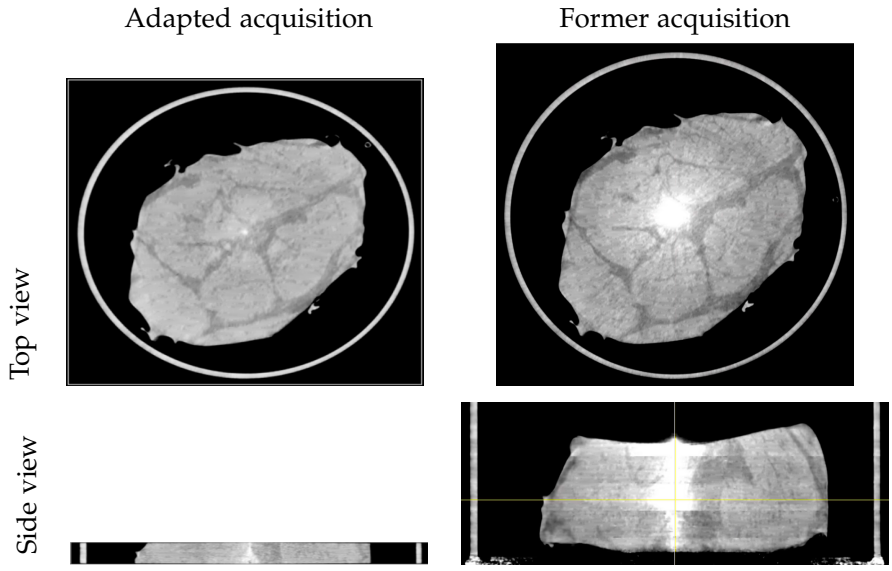

Figure 6.2: This figure contains images of the top and side views of the pig neck sample. On the left side are the results acquired with the adapted script and the right side images show the same results from section 2.4 with a Gaussian filter applied to it. The side view of the adapted acquisition is 12.5 mm (the vertical span of the field of view) and 75 mm on the right, which is six stacked measurements. The segment on the bottom left image is located at the middle of the side view on the right side. Both have a bright central artefact which is less broad on the adapted acquisition compared to the former one.

The result of this new acquisition scheme can be seen in figure 6.2.
The new acquisition greatly reduces the artefact in the central part compared

to the former one. However, both measurements still have a bright artefact at the rotation centre, where the artefact is more confined to the center for adapted acquisition as for the former one. The top view of the adapted acquisition shows a slightly brighter region around the center compared to the rest of the image similar in size to the spread of the central artefact on the right images. Even though this region still is brighter than the rest of the image, the contrast in that region is still good enough to clearly be able to tell the muscle and the fat apart from each other.

6.2 Improved Signal Retrieval

In this section the signal retrieval introduced in chapter 5 will be applied to the data set measured by the new adapted acquisition script from section 6.1 and compared to the results obtained with the separated signal retrieval and flat correction.

The signal retrieval of this sample was, despite flats with five times more exposure time, more difficult than for the former data. If the sinogram is averaged for each column we should get a curve which is approximately continuous aside from small fluctuations. This is the case for the sinogram of the signal retrieved data shown in figure 6.2. The combined signal retrieval and flat correction, however, shows some distinct discontinuities in its curve. The two curves are shown in figure 6.3.

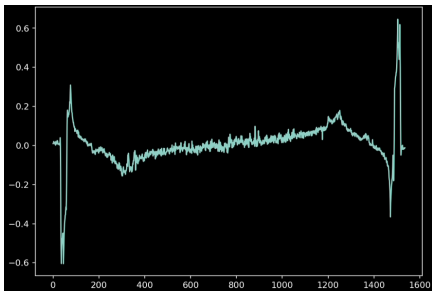

(a) The sinogram averaged for each column for the a separated signal retrieval and flat-field correction. The flat-field correction was done by averaging the two flats before and after the sample measurement. The curve has a continuous behaviour towards the middle region, despite some smaller peaks.

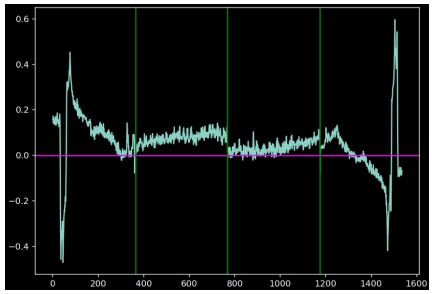

(b) The sinogram averaged for each column for combined signal retrieval and flat-field correction. The curve shows one clear discontinuity at the middle and two not so large shifts at the marked green columns. These columns also coincide with the grating gaps of g1 and g2.

Figure 6.3: The averaged sinogram curves show that the new signal retrieval has a continuity problem for this sample. Reconstructing the curve on the right results in strong artefacts and a low contrast. This can be fixed by shifting each of the four regions separated by the green lines with a constant shift, forcing it to be continuous. The result of this procedure can be seen in figure 6.4

The discontinuities in figure 6.3b can be manually corrected by adding a constant value to each quarter of the image separated by the grating gap locations on the image. Reconstructing the result of these manual shifts yields the reconstruction visible in figure 6.4. These images have again a

good central region compared to figure 6.2 but a ring artefact as it already appeared in figure 5.3. Since the grating gap regions do not only cause a shift between but also smaller shifts at its vicinity, the ring artefact is not removable by constant shifts on each quarter of the image. This procedure can be automated by matching the average values of the sinograms around the grating gaps.

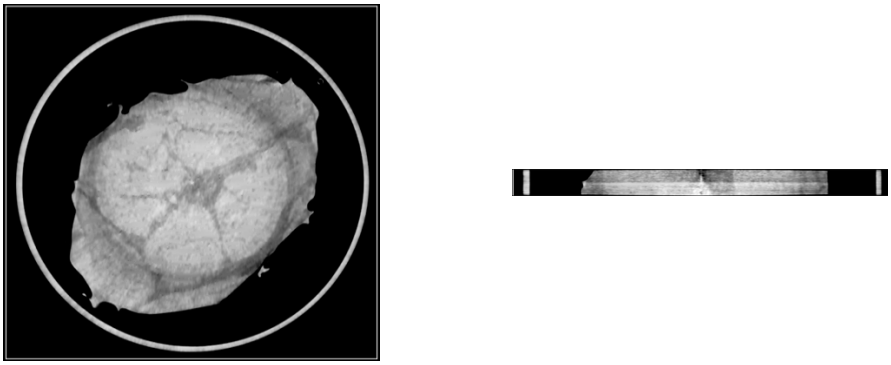

Figure 6.4: Reconstruction of the pig neck measurement with the adapted acquisition script and the combined signal retrieval and flat-field correction. The top view on the left has a good correction at the center and is almost artefact free while there is a ring artefact at the outer grating gaps of g2. The side view shows that central artefact is not only bright but shifts from dark to bright.

A closer look at the central region is taken in figure 6.5 reveals that the overall structures of both methods are the same. The new signal retrieval with the adapted sinogram, however, has no dominant central artefact. Especially compared to the old acquisition script the central region is greatly improved and shows features in the vicinity to the rotation centre. The new acquisition script also reveals a possible tissue contrast around the central region which before was covered by the artefact. The contrast is slightly visible on the top left and even better visible on the bottom left while the absorption image has no such feature. Within the scope of this work this claim was not investigated closer and would have to be remeasured or even confirmed through a biopsy but there has been proof that the phase contrast signal outperforms the absorption image [25].

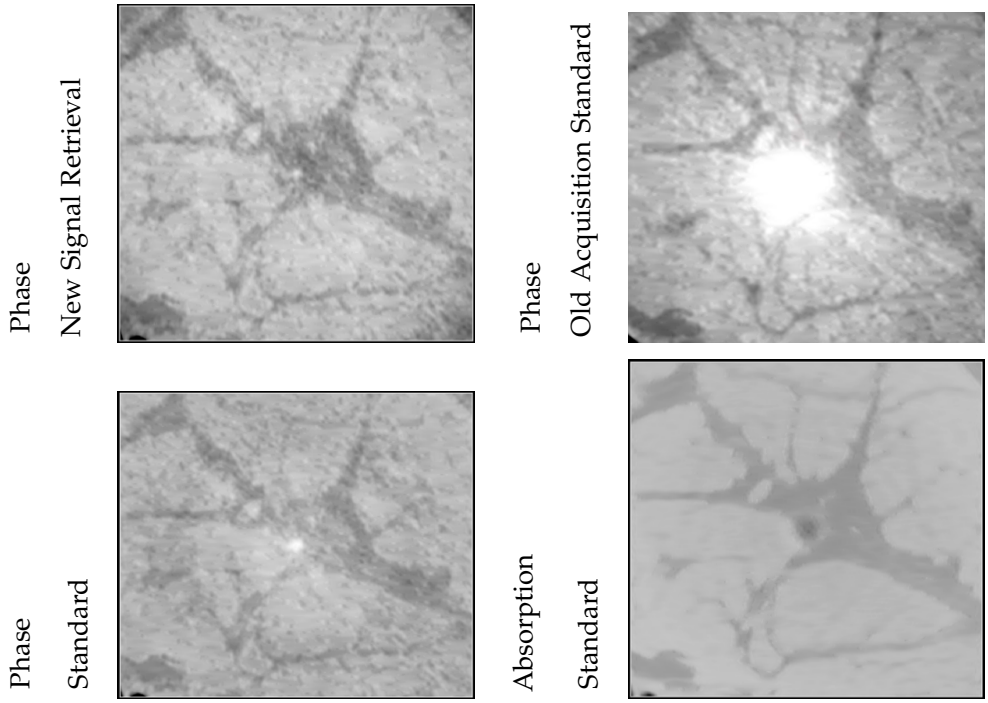

Figure 6.5: A zoom-in on the central region of the reconstruction of the adapted acquisition measurement with the two different signal retrieval and reconstruction methods. In addition an absorption image of the same region as well as the old acquisition script is shown for comparison. The data were filtered with a Gaussian filter (sigma of two in y and z direction) before the reconstruction.

6.3 Summary

The adapted acquisition model greatly improved the region at the vicinity of the artefact and reduced the stripe artefacts in the image due to the higher number of angles. Additionally, the shorter total acquisition time reduces the amount of time a measurement takes from over eleven to under nine minutes for a single vertical tomography segment. Small structures like thin filaments of tissue (see figure 6.5) are better visible on the adapted acquisition while the tissues are a bit more granular looking compared to the former acquisition which comes from the statistics reduction per projection which is higher for the 600 angle case compared to the 1000.
As the simulation showed, the strength of a fast acquisition is an easier correction if more parameters of the flat-field are known. This leads like the new signal retrieval to the question if the phase stepping can be done continuously to have the option to acquire some phase drift information constantly from the sides of the measurement where no sample is in the way. This will be investigated in the next chapter 7.

Chapter 7

Continuous G0 Movement

Moving the g0 during measurements has interesting applications, some of which were mentioned before in the form of constant monitoring the phase drift on areas without the sample. It can also reduce the exposure and acquisition time, as there is no need to wait for the g0 movement if it is moved during the measurement. It opens up new possibilities for the data acquisition for helical scans.

7.1 Feasibility

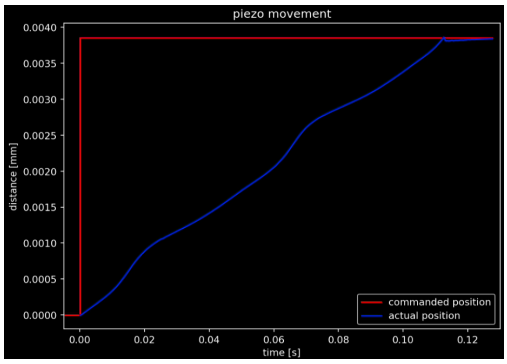

Figure 7.1: The curve of a piezo which is directed to a fixed distance. The time it takes the piezo to reach its goal of 5/6 of a phase curve period is around 0.115 seconds.

To be able to measure the phase curve, the phase stepping either needs to be changed into a continuous movement or fast enough stepping to get a new phase step position for each projection measured. For the acquisition

script introduced in section 2.2 it is necessary that g0 can be moved by one fifth of the period (one period is approximately 4 μm) at a rate of 10 Hz. If this is possible, the piezo motor can satisfy the requirements. Therefore as a first step the movement of the piezo motor of g0 was evaluated. The motor controller has the capability to log its position during a movement, up to 1024 points, into a data file. This data for a single piezo movement command is shown in figure 7.1. It was a movement commanded towards the location 3.8 μm away from its origin. It reached its target at around 0.115 seconds resulting in a velocity of approximately 33 μm per second. This is more than enough to do one phase step per 0.1 seconds as it would be required from the acquisition scheme from section 2.2 which requires only 8 μm per second (or 0.8 μm in 0.1 seconds as our frame rate is 10 Hz).

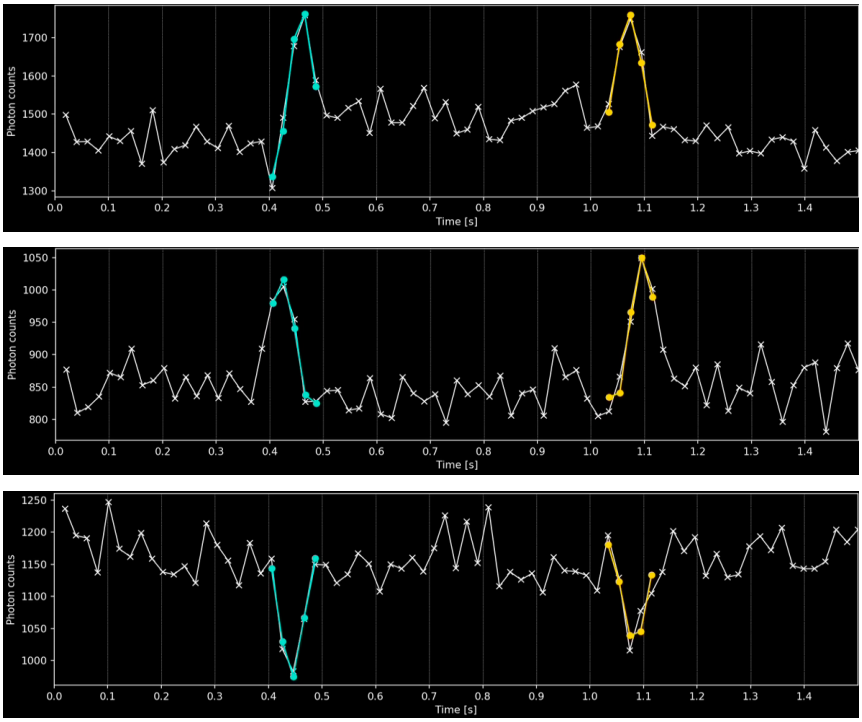

Figure 7.2: The photon counts of three different pixels over time where in between the g0 was moved for 4 μm in one direction and back again. To find the correct interval of the movement a sine fit over all possible intervals was done and the regions with the smallest errors to the actual measurements over all pixels chosen. The turquoise and yellow points show these regions and fits where turquoise is the forward movement and yellow the back movement. The measurement was done at a frame rate of 50 Hz and 70 kVp at 10mA.

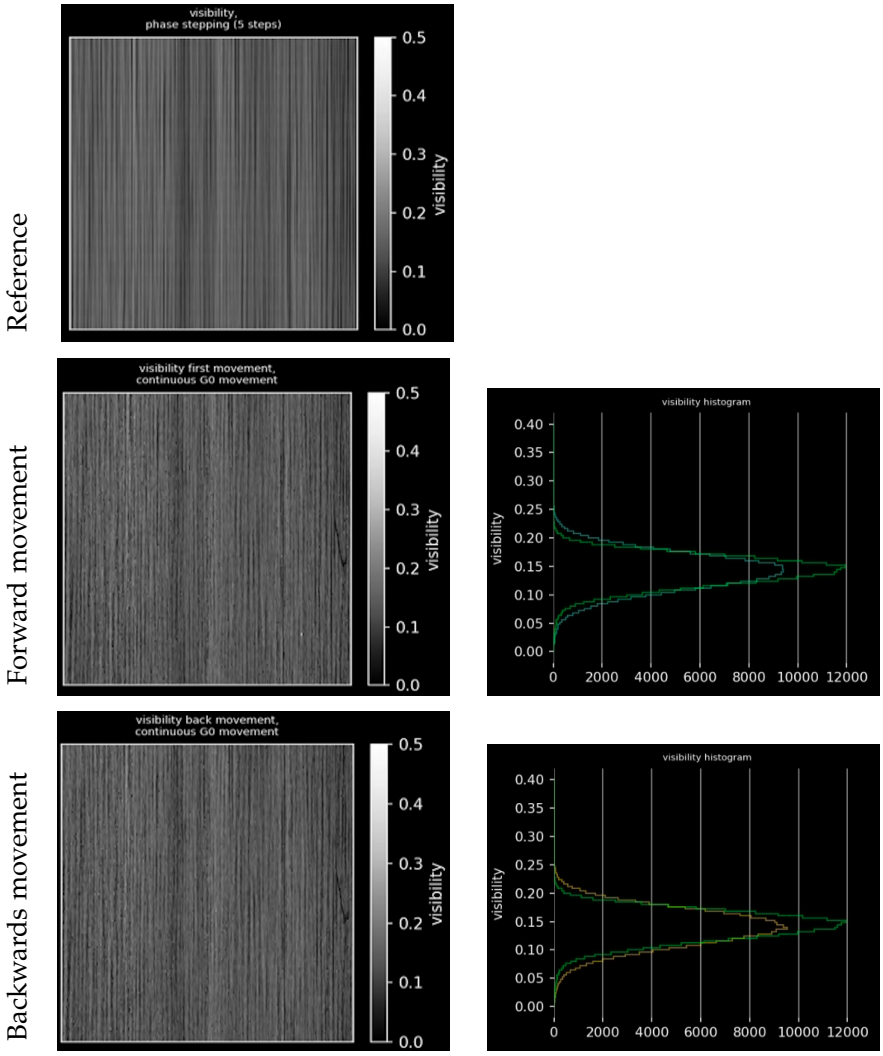

Figure 7.3: In the top row a reference visibility map of a phase stepping measurement is shown. Its histogram is layered on top of the other two visibility maps in green. On the second row the visibility map is shown to the left and the corresponding histogram in turquoise. On the bottom row the back movement visibility map is plotted to the left again with its corresponding histogram to the right. The measurement was done at a frame rate of 50 Hz, 70 kVp at 10mA and the piezo movement happened over 0.1 second each. The phase stepping flat has compared to that a 5.5 second longer exposure time.

The first test of a measurement with a moving g0 was done by measuring the flat-field at a rate of 50 Hz. The piezo was moved to a location a period away from its home position and back again during that time. This is a possible realisation of a continuous g0 movement. Since the controller only saves positions, there is no good reference point of when the g0 movement happens. The movement frames have to be found by error minimisation. The number of frames for the movement was found by repeating the following error minimization over multiple possible frame-ranges. Fitting one period of a sine to each interval of those frame-ranges and calculating the error to the points. By minimising this error we get two regions where the movement happened as well as the interval length. This can be seen on figure 7.2 where the optimal interval was 5 frames long. On the three curves, the fitted region is not always obvious and the region selection is also not the easiest. The movement is also not clearly defined on the frames as some of it might happen partially in the frame before and after. To reduce error sources as well as making the analysis easier the piezo movement script will later be combined with the image acquisition script. This will allow to coordinate the piezo movement properly and to prevent a wrong interval selection which could leads to artefacts.
If the movement interval has been located, these frames can then be signal retrieved to yield the flat-field parameter maps. The visibility map is related to the amplitude of the phase stepping curve and shows how much signal can be measured. They can be seen in figure 7.3 and show that the visibility map has a similar distribution for the histogram and therefore the signal strength of the phase curve for two methods is comparable. A similar result can be obtained from the phase images which are shown in figure 7.4. The two flats start from a different phase value in the phase stepping curve and are therefore shifted but otherwise identical except for some phase drift.

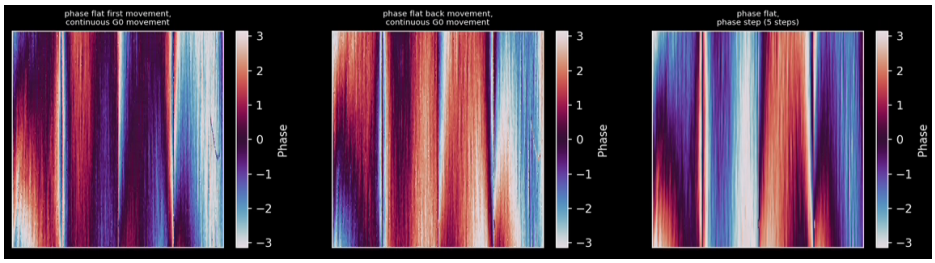

Figure 7.4: A comparison of the phase maps for the measurement of the continuous g0 movement. On the very left is the phase map of the forward movement, in the middle is the backmovement and on the right a reference phase flat. The measurement was done at a frame rate of 50 Hz, 70 kVp at 10mA and the piezo movement happened over 0.1 second each. The phase stepping flat has compared to that a 5.5 second longer exposure time.

This first test measurement was the only one with truly continuous movement. Since there is no way of changing the speed of the movement and a single move command can not sustain a full measurement of a tomography (due to the range of the piezo motor) the operating mode was changed to a fast phase stepping instead. With this approach there is not a real continuous movement any more but tomography measurements can be done by knowing the phase position at each projection measurement. With this method an ideal phase curve can be planned to make sure the phase curve is well probed. This will be discussed in the next section.

7.2 Model

In this section the movement pattern which was chosen for the piezo is introduced. For the following applications a fast phase stepping has been chosen to be the way of moving the piezo motor.
Since the requirement to get a good measurement is dependent on how well the phase curve can be fitted, the tomography needs to have for every angle all the phase information to do so properly. Therefore, a pattern which can yield the correct g0 position for all angles is necessary. One possible pattern to do this with equidistant phase curve sampling is a ”zig-zag” pattern illustrated in 7.5. It allows to have any amplitude for the pattern itself and to shift the pattern for each rotation by one phase step.

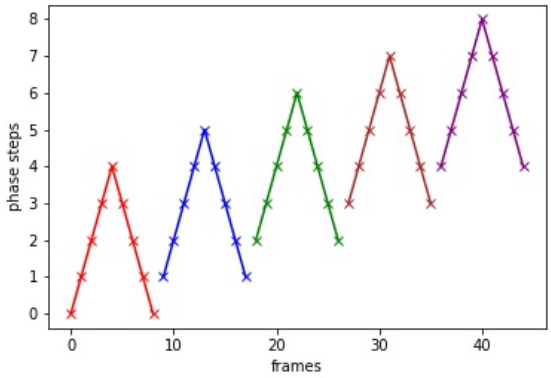

Figure 7.5: The zig-zag pattern for nine angles per rotation and five phase steps.

This pattern keeps the piezo in a safe range, the steps can be adapted arbitrarily, the phase parameter can be extracted constantly and it gives phase steps for each angle in order. The amplitude of this pattern can be changed

such that it is basically a straight movement with one direction change for a rotation to have a better phase drift analysis. The continuous movement will result in a more homogeneous visibility map as the grating will not only be used at certain points but over many periods, averaging out grating imperfections.

7.3 Results

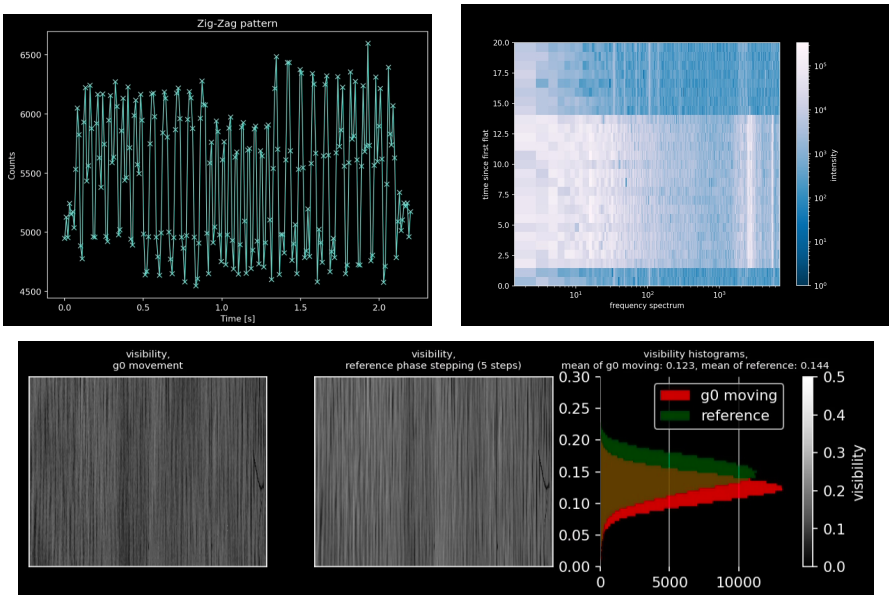

Figure 7.6: The top left image shows the photon count curve of a single pixel over time. On the top right is the vibration measurement of the system during this time-span. On the bottom row is to the left the visibility map of the ”zig-zag” movement, in the middle a reference visibility map of a phase stepping flat-field measurement and on the right is the comparison of the two histograms. The measurement was done at a frame rate of 10 Hz, 70 kVp at 10 mA and the piezo movement happened at 10 Hz. The ”zig-zag” pattern used 41 virtual angles and a amplitude of the pattern of five phase steps, each a fifth of the period.

The first measurement with this new ”zig-zag” pattern was a projection series done at 10 Hz for the detector and the piezo, with five phase steps per phase stepping curve and the 41 virtual angles. Virtual angles means that there was only a flat-field measured and no rotation involved but if a sample was in the beam the number of projections per rotation would have

been 41. The piezo movement is shown in figure 7.6 and was controlled by a separate script than the detector and x-ray source. The different ”rotation” pattern motions can be distinguished by eye as the curve changes its periodic behaviour. By taking points of the corresponding virtual angles the visibility map can be obtained and compared to a phase stepping flat measurement on the bottom of figure 7.6.
The visibility map for the movement on the bottom of figure 7.6 has a lower mean value compared to the reference. The mean value difference in figure 7.3 is equal which can be related to the movement type. For section 7.1 the movement was continuous but now it is a fast stepping which is not always the most accurate. Some points on the top image of figure 7.6 had some outliers and the movement is visually recognisable but not perfectly accurate. The mean value of the visibility ranges from 0.13 to 0.12 depending on the points that are picked. Here for the first time it is clearly visible that the piezo motor is not at all suited for a continuous movement but for alignment. On top of this the data of the vibration sensor can be analysed. On the top right of the figure 7.6 the frequency spectrum over time is shown. The movement can clearly be identified by the bright rows compared to the blue colors before and after. Despite the piezo not being designed for such a task, the visibility is still good enough for imaging.

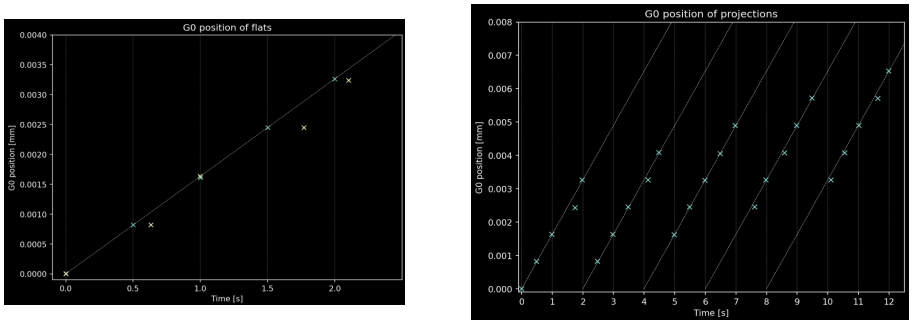

Figure 7.7: On the left side are two flat measurements from before and after the projections. On the right side is the projection measurement. The dotted lines show at which points in time a piezo movement should occur. Some movements lagged behind the schedule which is visible if the crosses are not on the intersections of the vertical lines and the dotted lines at an angle. The frame rate of the detector was 10 Hz and g0 was moved at 2 Hz.

To improve the data acquisition, for the next measurement the g0 movement script was integrated into the measurement program. With this change the start of the movement can be timed with the image acquisition such that no more fitting has to be done to find the start of the movement. It also

allows to perform full tomography acquisitions with multiple slices without desynchronising.
To test this new script and to see if a sample can be imaged a measurement of a projection with a sample has been done. The frame rate of the detector was set to 10 Hz and g0 was relocated at a rate of 2 Hz. Therefore for each movement is imaged with five frames. As for all the other measurements first a flat-field measurement is taken, then the sample is lifted into the beam, five measurements of the sample were taken and then the sample was removed from the beam again and a last flat was taken. These measurements are shown in figure 7.7.
As the figure 7.7 shows, for some movement commands, the script lagged behind and sent the commands up to 0.3 seconds too late. For a tomography measurement this would cause gaps in the phase stepping curve for the signal retrieval. This measurement was done such that 5 images per phase step were acquired and the projection was taken with a multiplicity of five where each measurement was shifted by one phase step. Therefore a good signal retrieval should still be possible. The phase images of the result have been shown in figure 3.2

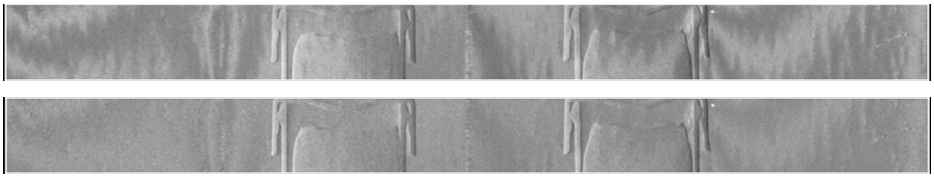

Figure 7.8: The phase channel of the flat-field corrected signal retrieval of the measurements shown in figure 7.7. On the top is the image of the movement frame while the bottom image is 0.3 seconds after the movement.

As the images on figure 7.8 show, the projection has arch-like artefacts over the phase image. These artefacts reduce when frames farther away from the g0 movement are used but they do not vanish completely.
As already mentioned the piezo motor is not really suited for the task of this measurement procedure. It is capable of adjusting an instrument very accurately but then keep it at that position rather than moving it all the time. If the piezo really causes these artefacts it should be possible to also see these patterns by simulating a timing inaccuracy of the piezo motor during measurement as will be discussed in the next section.

7.4 Simulation of Misalignment

To further explore if the behaviour in figure 7.8 can be explained by an inaccurate g0 control by simulation a timing inaccuracy of g0 resulting in a slight misalignment. In the simulation the same model and background flats as for section 4 were used but the phase array was changed while assuming the points to be at the ideal value for signal retrieval. This was done for various randomly chosen values constrained to a certain distance from the original point. The result of this simulation can be seen in figure 7.9.

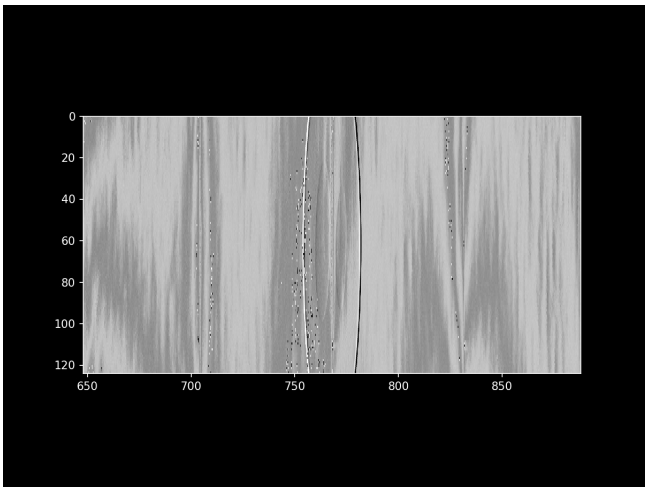

Figure 7.9: Simulation of a phase curve signal retrieval with a g0 misalignment. The misalignment was chosen randomly with a upper and lower limit of a fifth of a phase step ($\frac{\pi}{25}$). The phantom was as in section 4 the SheppLogan3D with the same size and attenuation and refraction sinograms.

The simulation has been done for various background flats and maximum misalignment limits. The artefact pattern changed in intensity but not much in shape (the image of the simulation is upside down compared to the data ones). Therefore it can be concluded that it is possible to perform measurements with a constantly moving piezo as long as the control is accurate in the temporal regime. It is advised to exchange this motor with a servo-motor like the M-230 by ”Physik Instrumente”.

Chapter 8

Conclusion

In this thesis several aspects concerning the optimization of a wide-field-of-view phase-contrast computed-tomography setup were investigated. The improvements that were done throughout this thesis lie in the reduction of acquisition time, reduction of the spread from the central bright artefact and the correction of a phase mismatch. Furthermore, it was shown that g0 can be moved during the data acquisition.

At the beginning of the thesis it was shown that the flat field correction significantly influences the artefacts that are visible in the reconstruction. Figure 3.6 illustrates this behaviour by changing the brightness of the central artefact solely by changing the flat field correction. By this observation, also a piece-wise linear interpolation between flats is possible but finding the correct intervals for which a new flat is required has no straight forward answer. This might be partially solved by a continuous g0 movement. As a few columns at the side of the detector do not have a sample in the beam these could in principle give some insight on the drift parameters for the outer two grating regions, where the inner regions drift correlates to the outer ones. With that it might be possible to decide during measurement at which temporal positions a new flat would be necessary. In addition to that the new signal retrieval method as well as the altered acquisition scheme could benefit from these parameters immensely.

The simulation was able to predict artefacts that were observable in the reconstructed data and therefore link cause to artefact. This was possible for the period mismatch and could also show that the bright artefact in the middle is not the result of a incorrect flat correction entirely. It hinted that a fast phase stepping curve acquisition decreases the artefacts imposed by the flat field correction and will benefit more from a better flat field correction compared to a slow phase curve acquisition.

The combination of the signal retrieval and flat field correction was shown to

work. The linear interpolation between the two flats is not giving a perfect correction and results in different artefacts overall, especially a ring artefact at the position of the outer g2 gratings reduces the quality of the reconstruction. The signal retrieval often has row wise discontinuities which happen at the grating positions and need to be removed before the reconstruction.

The adapted acquisition script could reduce the middle artefact greatly and measured a before unobservable separation of fat tissue (neither in the old acquisition scheme nor in absorption), while reducing the acquisition time by around 19 %. This observation still needs to be confirmed by additional examination of the sample (offset to rotation centre or biopsy).

Lastly the continuous g0 movement during measurement could be shown to work even for the simplistic approach in this thesis. The difference between the constantly moving measurement and the fast phase stepping could also be seen in the mean value of the visibility map shown in the tables 7.3 and 7.6 where for the constantly moving case the visibility mean value was as high as for the phase stepping measurement under ideal conditions (waiting for g0 and high statistics) where for the fast phase stepping the value dropped up to 0.02 (around 8-15%). This was achieved with a piezo motor that is not supposed to be used as a constantly moving driver. With a piezo motor dedicated for this task the continuous flat-field parameter extraction could be further investigated to obtain a fully adaptive flat-field measurement script.

Bibliography

[1] Max Roser, Esteban Ortiz-Ospina, and Hannah Ritchie. Life expectancy. *Our World in Data*, 2013. https://ourworldindata.org/life-expectancy.

[2] GBD 2017 Causes of Death Collaborateurs. Global, regional, and national age-sex-specific mortality for 282 causes of death in 195 countries and territories, 1980–2017: a systematic analysis for the Global Burden of Disease Study 2017. *Lancet*, 392(10159):1736–1788, 11 2018.

[3] Federal Statistical Office Christoph Junker. Death and its main causes in Switzerland, 2016, January 2019.

[4] J. Ferlay et al. Estimating the global cancer incidence and mortality in 2018:GLOBOCAN sources and methods. *International Journal of Cancer*, 144:1941–1953, 2018.

[5] Howlader N et. al. Seer cancer statistics review. National Cancer Institute. Bethesda, MD, April 2020.

[6] Gapminder. Four income levels, March 2018.

[7] Institute for Quality and Efficiency in Health Care. The breast cancer screening program in Germany, February 2018.

[8] Rupali Swain Sumant Ugalmugle. Mammography Systems Market Size By Product (Analog Systems, Full Field Digital Mammography Systems FFDM, Breast Tomosynthesis Systems), By Technology (Screen Film, 2D Mammography, 3D Mammography), By End-use (Hospitals, Ambulatory Surgical Centers), Industry Analysis Report, Regional Outlook, Application Potential, Competitive Market Share and Forecast, 2019 – 2025. Global Market Insights, November 2019.

[9] Mammography Systems Market by Type (Analog Mammography Systems, Digital Mammography Systems and Breast Tomosynthesis Systems), By Technology (2D Mammography, 3D Mammography and Combined 2D and 3D Mammography) and by End Users for Hospitals, Ambulatory Surgical Centers, Educational and Research Institutes and Diagnostic Centers: Global Industry Perspective, Comprehensive Analysis and Forecast, 2017 - 2023. Zion Market Research, April 2018.

[10] American cancer society guidelines for the early detection of cancer, May 2018.

[11] Bernard W. Steward and Christopher P. Wild. *World Cancer Report 2014*. International Agency for Research on Cancer, 2014.

[12] Yojana V Nalawade. Evaluation of breast calcifications. *Indian Journal of Radiology and Imaging*, 19(4):282–286, November 2009.

[13] J. H. Hubbell and S. M. Seltzer. X-Ray Mass Attenuation Coefficients. NIST Standard Reference Database 126, July 2004.

[14] Di Maria S et al. Optimal Photon Energy Comparison Between Digital Breast Tomosynthesis and Mammography: A Case Study. *Phys Med.*, 30(4):482–488, Feburary 2014.

[15] Andreas Maier, Stefan Steidl, Vincent Christlein, and Joachim Hornegger. *Medical Imaging Systems*. Springer Open, 1973.

[16] Myun-Sik Kim and Toralf Scharf et al. Talbot images of wavelength-scale amplitude gratings. *Optical Society of America*, 2012.

[17] Wen H. *Biomedical X-Ray Phase-Contrast Imaging and Tomography*. Springer, Cham, 2019.

[18] Peter Ullrich. Johann Radon und die Grundlagen der Computertomographie. *Mathematische Semesterberichte*, 50:143–166, 1004.

[19] Lucia Romano and Marco Stampanoni. Microfabrication of X-ray Optics by Metal Assisted Chemical Etching: A Review. *micromachines*, 11(6), 06 2020.

[20] W. van Aarle, W. J. Palenstijn, J. Cant, E. Janssens, F. Bleichrodt, A. Dabravolski, J. De Beenhouwer, K. J. Batenburg, and J. Sijbers. Fast and Flexible X-ray Tomography Using the ASTRA Toolbox. *Optics Express*, 24(9), 2016.

[21] W. van Aarle, W. J. Palenstijn, J. De Beenhouwer, T. Altantzis, S. Bals, K. J. Batenburg, and J. Sijbers. The ASTRA Toolbox: A platform for advanced algorithm development in electron tomography. *Ultramicroscopy*, 157:35–47, 2015.

[22] Schlomo Engelberg. *Digital Signal Processing. Signals and Communication Technology.* Springer, London, 2008.

[23] Gürsoy D, De Carlo F, Xiao X, and Jacobsen C. Tomopy: a framework for the analysis of synchrotron tomographic data. *Journal of Synchrotron Radiation*, 21(5):1188–1193, 2014.

[24] Pelt D, Gürsoy D, Palenstijn WJ, Sijbers J, De Carlo F, and Batenburg KJ. Integration of tomopy and the astra toolbox for advanced processing and reconstruction of tomographic synchrotron data. *Journal of Synchrotron Radiation*, 23(3):842–849, 2016.

[25] Georg Schulz, Timm Weitkamp, Irene Zanette, Franz Pfeiffer, Felix Beckmann, Christian David, Simon Rutishauser, Elena Reznikova, and Bert Müller. High-resolution tomographic imaging of a human cerebellum: comparison of absorption and grating-based phase contrast. *Journal of Synchrotron Radiation*, 23(3):842–849, 2016.